Modeling of EPR parameters for Cu(II). Application to the Selective Reduction of NOx catalyzed by Cu-zeolites

Estefanía Fernández, Marta Moreno-González[†], Manuel Moliner, Teresa Blasco, Mercedes Boronat and Avelino Corma*

Instituto de Tecnología Química (UPV-CSIC), Universitat Politêcnica de Valencia – Consejo Superior de Investigaciones Científicas, Avda. de los Naranjos s/n, 46022 Valencia, Spain.

[†]Present address: Department of Chemistry, The University of British Columbia, 2036 Main Mall, Vancouver, British Columbia V6H1Z1, Canada

*To whom correspondence should be addressed acorma@itq.upv.es

1

Abstract

We present a combined theoretical – experimental study aiming to provide information about the location and coordination environment of the Cu^{2+} species involved in the selective reduction of NOx with NH_3 catalyzed by Cu-zeolites. From the experimental side, we show and discuss the EPR spectra of the three molecular sieves most widely used as catalysts for the NH_3-SCR-NOx reaction, namely Cu-SSZ-13, Cu-SAPO-34 and Cu-ZSM-5 both in their hydrated state and after dehydration. Then, we investigate the EPR spectra of Cu-SSZ-13 and Cu-SAPO-34 under the following conditions: i) after NH_3 adsorption, ii) after NO addition, and iii) in the presence of a NO/O_2 mixture. As regards the theoretical part, an exhaustive computational study has been performed that includes geometry optimization and calculation of the EPR parameters of all the relevant systems involved in the NH_3-SCR-NOx reaction. The influence of local geometry and Al/Si distribution in the zeolite framework on the EPR parameters and the most probable location of Cu^{2+} in each material are analyzed, and assignations of the EPR signals obtained under different reaction conditions are discussed.

Keywords

Cu-zeolites, theoretical modelling, EPR, NH_3-SCR-NOx reaction, DFT

1. Introduction

Nowadays, there is a high concern in the growing world-wide energy demand, as well as in the global warming coming from increasing fossil fuel combustion and CO_2 emissions. Diesel engines offer the great advantage of being more fuel-efficient than the classical gasoline ones, contributing to lower CO_2 emissions. However, they are primary emitters of other contaminants such as particulate matter or nitrogen oxides. In particular, NOx emissions provoke the photochemical smog phenomena in big cities, which implies a serious health hazard for the population. The NOx problematic lies on the low efficiency of the three-way catalyst (TWC) used conventionally in gasoline vehicles, to reduce NOx under the oxidative exhaust gases coming from lean-burn engines. In this sense, there has been an extensive research over more than 20 years on new processes to reduce NOx emission from diesel vehicles. It was in 2005 when the Selective Catalytic Reduction (SCR) of NOx with NH_3 was firstly applied in Europe on heavy duty vehicles, forced mainly by more stringent EU emission laws. Later on, it was also implemented in light duty vehicles and other non-road vehicles both in Europe and USA. Indeed, this process seems to be the most promising alternative to lower NOx emissions and comply with actual and future emission laws. [1, 2]

Vanadia-based catalysts were firstly employed, as they were conventionally applied for the NH_3-SCR-NOx reaction in stationary sources, but they showed low conversions at low temperatures and low thermal stability when applied on mobile sources. The main alternative found are zeolite catalysts exchanged with transition metal ions, mainly Fe and/or Cu, which display high conversion in a wide range of temperatures, and specially Cu-zeolites, which are highly active at low temperatures. [3-6] In 2010 Kwak *et al.* [7] reported for the first time in academia literature a Cu-SSZ-13 zeolite that, besides being highly active and selective in the NH_3-SCR of NOx, does not suffer from the low hydrothermal stability of Cu-ZSM-5. Hydrothermal stability is an indispensable feature, since temperatures of 750°C are reached in the regeneration of the upstream DPF (Diesel Particle Filter). For this reason, Cu-SSZ-13 has already been commercialized and implemented as SCR catalyst both in USA and Europe.

The selective catalytic reduction (SCR) of NOx with NH_3 in the presence of O_2 occurs according to:

$$4\,NH_3 + 4\,NO + O_2 \rightarrow 4\,N_2 + 6\,H_2O$$
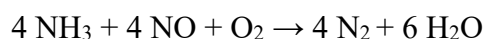
The reaction mechanism on Cu-SSZ-13 zeolite and its isostructural silicoalumino-phosphate Cu-SAPO-34 has been widely investigated in the last seven years, and a redox

catalytic cycle involving a change in the oxidation state of copper has been established (see Scheme 1). In the oxidation half-cycle Cu^+ is oxidized to Cu^{2+} by reaction of NO with O_2, forming nitrite (Cu^{2+}-NO_2^-) and nitrate (Cu^{2+}-NO_3^-) species. Then, in the presence of NO and NH_3, Cu^{2+} is reduced to Cu^+ producing N_2 and H_2O, thus closing the catalytic cycle.
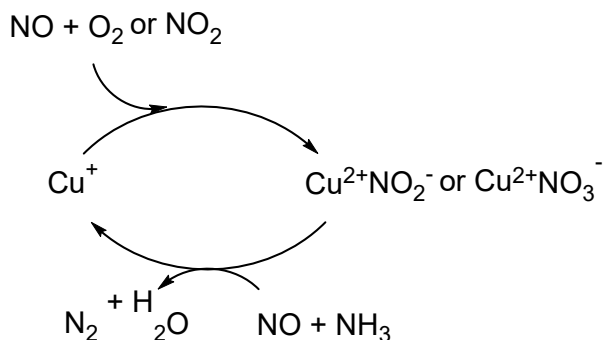
Scheme 1. Proposed mechanism for the NH_3-SCR-NOx reaction catalyzed by Cu-zeolites.

Isolated Cu^{2+} cations preferentially located in the plane of six-membered ring (6R) units have been identified as the active sites in Cu-SSZ-13 zeolite and, on the basis of their common CHA framework structure, the same position has been assumed for Cu^{2+} in Cu-SAPO-34. [8, 9, 10] Similarly, Cu^{2+} cations tend to coordinate to 6MRs in Cu-ZSM-5 zeolite, but due to the low symmetry and large number of non-equivalent T sites in MFI structure there is not a unique specific position for Cu^{2+} in this material. [11, 12]

Electron Paramagnetic Resonance (EPR) spectroscopy is a very sensitive technique that allows the observation of isolated paramagnetic Cu^{2+} species at very low concentration. It provides, on the one hand, quantitative data regarding the total amount of EPR-active Cu^{2+} sites present and, on the other hand, structural information about their coordination environment. *In situ* or operando EPR experiments in the presence of reaction gases tell us about the change in the oxidation state of copper during the reaction, or about the type and number of reactant molecules that preferentially interact with Cu^{2+} sites.[13-15] However, and despite the unquestionable value of these data, often different framework positions and/or adsorbed molecules produce similar coordination structures around Cu^{2+}, making unequivocal assignations harder to obtain. For this reason, it would be desirable to combine the experimental EPR data with reliable theoretical modelling of the Cu^{2+} species present in Cu-zeolites and their corresponding EPR signals. In this sense, only a few computational studies have been reported in the literature [16, 17, 18, 19] and they

have been so far unable to reach definitive conclusions about the unambiguous assignation of the EPR signals. Thus, in the present work we try to shed some light into this matter by combining the experimental EPR spectra of Cu-SSZ-13, Cu-SAPO-34 and Cu-ZSM-5 catalysts under different conditions with a systematic computational calculation of the EPR parameters of the possible structures present. The most probable location of Cu^{2+} in the dehydrated zeolites and the assignations of the EPR signals obtained in the presence of NH_3, NO and a NO/O_2 mixture are discussed.

2. Experimental Section

2.1. Preparation of Cu-zeolites

Zeolite Cu-ZSM-5 was obtained by classical ion exchange of H-ZSM-5, obtained by calcination at 580 ºC of commercially available NH_4^+-ZSM-5 (TZP-302 A), with 250 ml of a 2 mM aqueous solution of $Cu(CH_3COO)_2 \cdot 4 H_2O$ per gram of zeolite and stirring for 24 h at room temperature.

Zeolite Cu-SSZ-13 was prepared by one-pot direct synthesis using a method developed by our group and described previously, [20] from a synthesis gel of chemical composition: SiO_2 : 0.062 Al_2O_3 : 0.1 Na_2O : 0.06 Cu-TEPA : 0.15 TMAdaOH : 21 H_2O, being Cu-TEPA: copper-tetraethylethylenepentamine, and TMAdaOH: N,N,N-trimethyl-1-adamantammonium hydroxide. The gel was introduced into an autoclave with a Teflon liner and heated at 150 ºC under static conditions for 14 days. The resulting crystalline products were filtered and washed with water, dried at 100 ºC, and then calcined at 550 ºC in air to remove the occluded organic material.

Cu-SSZ-13-int material was obtained by classical ion exchange of a SSZ-13 zeolite synthesized using a previously described method [21], following the same ion-exchange procedure described above for Cu-ZSM-5.

Cu-SAPO-34 material was also prepared by one-pot direct synthesis using a method developed by our group and described previously, [22] from a synthesis gel of chemical composition: 0.19 SiO_2 : 0.5 Al_2O_3 : 0.4 P_2O_5 : 0.045 Cu-TEPA : 0.855 DEA : 18 H_2O, being DEA: diethylamine. The gel was introduced into an autoclave with a Teflon liner containing SAPO-34 seeds as well, and heated at 150 ºC under static conditions for 5 days. The resulting crystalline products were filtered and washed with water, dried at 100 ºC, and then calcined at 550 ºC in air to remove the occluded organic material.

The chemical composition of the obtained materials was analyzed by ICP-O ES (Varian 715-ES), and the results are reported in Table S1.

2.2. EPR experiments

About 20 mg of Cu-zeolite was placed into a 5 mm EPR quartz tube adapted to a high vacuum valve, connected to a vacuum line and dehydrated under dynamic vacuum at 450 °C (1 h) reaching a final pressure of ~10^{-6} mbar. Next, 99.9% isotopically labeled $^{15}NH_3$, ^{15}NO, or $^{15}NO/O_2$ were adsorbed at -196 °C by admitting onto the Cu-zeolite the desired amount of gas using a calibrated volume. Finally, when appropriate the sample in the quartz tube was heated (Tr) or degassed (Tv) at temperatures between 25 – 450 °C under controlled atmosphere.

EPR spectra were recorded with a Bruker EMX-12 spectrometer, operating at the X-band, with a modulation frequency of 100 KHz and amplitude of 1.0 Gauss. Spectra were measured at variable temperatures (-170 – 250 °C) using a Variable Temperature Accessory working with liquid or gas N_2 depending on the temperature of measurement.

2.3. Theoretical background

There is a wide variety of computational methodologies for the calculation of EPR parameters, whose precision and computational cost depend on the choice of the Hamiltonian, the inclusion and treatment of relativistic effects and electron correlation, and on the appropriate description of both valence and core electrons. [23] Depending on the way in which scalar-relativistic and spin-orbit coupling (SOC) effects are accounted for, there are different approximations to the four-component Dirac Hamiltonian. The so-called 'one-component' approaches introduce the SOC as a perturbation and calculate the spin-Hamiltonian parameters **g** and **A** as second-order derivatives of the selected reduction to the relativistic Hamiltonian. Since the magnitude of the SOC increases with increasingly heavier elements, the questionability of a perturbational approach gave rise to 'two-component' approaches, where the SOC is included in the orbital optimization step and thus calculated variationally, with the EPR parameters obtained then as first derivatives of the total energy. Finally, four-component approaches have been developed recently, although they are very expensive and only calculations on small systems have been reported so far [24, 25, 26] Given that Cu^{2+} is a 3d transition metal for which the relativistic contributions should be moderate, and considering that the present study requires the calculation of the EPR parameters of many possible structures, we employed the computationally affordable one-component approach with the Breit-Pauli Hamiltonian as implemented in the ORCA program [27, 28, 29, 30]. This approach can

be combined with different treatments of the electron correlation and, based on a good balance between computational cost and accuracy, calculations have been done at the DFT level employing the hybrid B3LYP functional, which shows a good overall performance for the calculation of EPR parameters, [31] and has been shown to reproduce experimental trends in copper complexes. [32]

Using this methodology, both the *g*-tensor and the hyperfine couplings *A* are expressed as sums of contributions:

$$g = g_e + \Delta g^{RMC} + \Delta g^{GC} + \Delta g^{(OZ/SOC)} \tag{1}$$

$$A = A^{FC} + A^{SD} + A^{SOC} \tag{2}$$

g_e is the value of *g* for the Zeeman effect of a free electron (~2.0023), whereas it is the other contributions what cause its deviation from that value in any other system. RMC and GC stand for relativistic mass correction and gauge correction, respectively, while the last term, called orbital-Zeeman/spin orbit coupling cross term, is the paramagnetic spin-orbital contribution, and it is the main contribution to the g-tensor. Unfortunately, it is also the most difficult to calculate accurately, and so far all functionals underestimate it, due to the combination of them providing too covalent bonding and two high d-d transition energies. Increasing the amount of HF exchange in the functionals seem to improve the results, but doing so can lead to a high spin contamination, and in general consolidated hybrid functionals such as B3LYP are preferentially recommended [33]

As to the hyperfine values, FC stands for Fermi contact, which is an isotropic term that depends on the spin density in the core s orbitals at the nucleus (the Cu^{2+} ion in our case); SD stands for spin-dipolar interaction, which represents the interaction between the magnetic moment of the nucleus with the magnetic moment of the electron, and the last term is the contribution from spin-orbit coupling. The SOC contribution is related to that of the g-tensor and a similar underestimation is expected. The spin-dipolar contribution can also be underestimated due to the excessively covalent description of DFT that favors the distribution of the spin-density of the valence shell, but should be reasonable if hybrid functionals are employed. The Fermi contact term is underestimated because it also depends on the effect of spin-polarization on the core orbitals of the nucleus due to the spin density in the d-orbitals, which is difficult to calculate accurately depending on the metal [34] Since the three terms can contribute with large values of opposing signs, and also arise from different properties difficult to correct at the same time, it is difficult to obtain accurate predictions for the hyperfine couplings.

Therefore, based on all of this and on previous reported results for Cu^{2+} species, we expected and obtained a systematic underestimation for the $g_\parallel$ parameters and reasonable albeit sometimes mixed results for $A_\parallel$, which nevertheless allow consistent comparisons of trends with the experimental data. The resulting average deviations for the calculated EPR parameters in the complete assignation of computational values to experimental signals is of 0.097 ± 0.013 for $g_\parallel$ and of 11 ± 29 for $A_{\parallel,Cu}$, as can be seen in Figure S1 in the Supporting Information.

2.4. Computational details

Since the relative dispositions of the ligands directly bound to Cu^{2+} can change its spectroscopic parameters, we firstly optimized the geometry of the whole system using a periodic approach, which provides more representative models of the catalysts. Cluster models were then cut out from the periodic optimized structures and the dangling bonds saturated with hydrogens, and a second geometry optimization was carried out in which only the terminal hydrogens were allowed to relax. Both geometry optimizations were carried out at the DFT level with the VASP code [35, 36], using the PW91 functional of Perdew and Wang [37]. A kinetic energy cutoff of 450 eV was set for the plane-wave basis set expansion of the valence density, whereas core electrons where considered by means of the projected augmented plane wave (PAW) formalism [38]. Integration in the reciprocal space was carried out at the Γ k-point for the Brillouin zone. The optimized cell parameters for each catalyst are $a = 13.803$, $b = 13.803$, $c = 15.075$, $\alpha = 60°$, $\beta = 120°$, $\gamma = 90°$ for SSZ-13 and SAPO-34, and $a = 20.090$, $b = 19.737$, $c = 13.142$, $\alpha = \beta = \gamma = 90°$ for ZSM-5. Several calculations were initially made to assess the size convergence of the approach (see Figure S2 and Table S2 in the Supporting Information). It was found that reducing the system strictly to the 6-ring of each site produces a noticeable change in $g_\parallel$ or $A_\parallel$ in some cases, and thus we selected the next bigger clusters, which in addition had the advantage of allowing the calculation of different catalyst compositions and Al or Si distributions without the need of dealing with cluster charges.

The EPR parameters **g** and **A** were then obtained from a third calculation on these cluster models at the B3LYP level, [39, 40, 41] using the one-component approach with the Breit-Pauli approximation as implemented in the ORCA program [27-30], which employs the coupled-perturbed SCF methodology by Neese [29]. For the Spin-Orbit Coupling (SOC), the recommended complete mean-field spin-orbit (SOMF) operator was used

[42], with the resolution of the identity (RI) approximation [43] and local DFT correlation included. Since the basis set must be flexible enough, the dedicated IGLOIII basis set [44] was chosen for all elements except copper, for which the recommended CP(III) basis set [45, 46] was employed instead. In addition, the integral accuracy for this center was increased up to 9. The SCF convergence criteria and integration grid were increased by means of the TightSCF and Grid5 options, respectively. Finally, although the gauge dependence is thought to be small, we selected the center of charge as the origin of angular momenta in order to minimize it.

3. Results and discussion

The EPR signals of the Cu^{2+} species in zeolites are usually axially symmetric and will be described here by $g_{||}$ and $A_{||}$ since the hyperfine structure is not resolved in the perpendicular region and all of them have similar $g_\perp$ values. As mentioned in the theoretical background section, there is a systematic underestimation for calculated $g_{||}$ of about 0.097 which anyhow allows making consistent comparisons of trends with the experimental data.

3.1. Hydrated Cu-catalysts

In general, all experimental studies on the EPR spectra of hydrated Cu-zeolites at room temperature report an isotropic signal that is very similar to the one observed for copper in aqueous solution, with $g_{iso} = 2.16$-2.17. [15] In the hydrated zeolites, water molecules directly bind to the Cu^{2+} ions, making them lose their coordination to the oxygens of the zeolite framework (O_f) and displacing them towards a wider space, i.e. a pore or cavity, where the $Cu^{2+}(H_2O)_n$ complexes can move freely. At lower temperature, however, anisotropy is observed due to some loss of degrees of freedom associated to restricted movement, and again a very similar signal with $g_{||} = 2.38 - 2.40$, $A_{||} = 425 - 460$ MHz and a $g_\perp$ of about 2.07 is reported for all zeolites [3, 15] The EPR spectra of hydrated Cu-SSZ-13, Cu-SAPO-34 and Cu-ZSM-5 recorded at -170ºC shown in Figure 1 are fully consistent with this signal, which we call **A,** that is usually assigned to Cu^{2+} species in a tetragonally elongated 5- or 6-coordination, i.e. with a square pyramidal or octahedral geometry. Although signal **A** is by far the most common feature observed in hydrated samples, contributions from other signals have sometimes been reported [47]. In fact, in the EPR spectrum of hydrated Cu-SSZ-13, we observe a different unassigned signal,

which we call **B**, with higher $g_\parallel$ and lower $A_\parallel$, that has also been observed in Cu-FAU [48] (Figure 1a). The $g_\parallel$ and $A_\parallel$ parameters obtained experimentally and from the computational simulations of the possible $[Cu(H_2O)_n]^{2+}$ complexes are given in Table 1, and the corresponding optimized structures are depicted in Figure 2.

Overall, and in agreement with previous work [16, 32. 49], octahedral complexes (structures **1-3** in Figure 2 and Table 1) provide the best assignment to signal **A**, with the rest of the systems (structures **4** and **5**) showing too low values for $g_\parallel$ and, in some cases, too large values for $A_\parallel$. Our calculations on octahedral $[Cu(H_2O)_6]^{2+}$ complexes evidence the sensitivity of the EPR technique to relatively small changes in the internal symmetry of the complex (see Table S3 for geometry details). Indeed, the elongation of one of the axial Cu-O bonds, i.e. a change towards a square pyramid structure, produces a decrease of $g_\parallel$ in structure **3**, more similar now to that of the 5-coordinated square pyramid structure **4.** On the other hand, structure **1**, with elongated axial bonds and unequal equatorial bond distances, i.e. providing a slightly rhombic signal of three different values in the *g* and *A* tensors, has a lower value of $A_z \approx A_{\parallel\parallel}$. Interestingly, the parameters of this latter $[Cu(H_2O)_6]^{2+}$ complex are more similar to those of signal **B**. Thus, these results suggest that while signal **A** is indeed caused by octahedral $[Cu(H_2O)_6]^{2+}$ complexes with C_i or C_1 symmetry (structures **2** and **3**), the appearance of signal **B** could be related to the stabilization of structures similar to the D_{2h} complex (structure **1**) on some zeolites under certain conditions.

3.2. Dehydrated zeolites.

Upon dehydration, Cu^{2+} cations lose their coordination sphere of water molecules and interact with the oxygen atoms of the zeolite framework directly bonded to Al, giving rise to the appearance of new EPR signals. The distribution of Cu^{2+} cations in each zeolite and therefore the values of the EPR *g* and *A* parameters measured depend on multiple factors such as zeolite structure, Si/Al ratio and distribution, copper loading, synthesis procedure, post-synthesis treatments, and method used to introduce the Cu^{2+} cation.

Dehydrated Cu-SSZ-13 and Cu-SAPO-34

Figure 3 shows the EPR spectra of Cu-SSZ-13, Cu-SAPO-34 and Cu-ZSM-5 after dehydration at 450ºC, following the procedure described in the Experimental Section. The key role of the synthesis procedure on the copper species present is clearly seen when

comparing the spectra in Figure 3a and 3b. Only one signal, labelled **C**, is observed in the Cu-SSZ-13 sample obtained by direct synthesis using Cu-tetraethylenepentamine (Cu-TEPA) complex and N,N,N-trimethyl-1-adamantammonium as organic structure-directing agents [20] whereas a second one, labelled **D**, is also seen in the spectrum of the same material obtained by the classical ion-exchange method. The EPR parameters of signals **C**, $g_{||} = 2.347$ and $A_{||} = 493$ MHz, and **D**, $g_{||} = 2.386$ and $A_{||} = 384$ MHz, agree with the results reported in previous publications ($g_{||} \sim 2.34$ and $A_{||} = 491 - 550$ MHz for **C**, and $g_{||} \sim 2.38 - 2.39$ and $A_{||} = 408 - 450$ MHz for **D**) [50, 51, 52] Previous studies on Cu-SAPO-34 report analogous signals, that is, signal **C** with parameters $g_{||} \sim 2.34$, $A_{||} = 481 - 504$ MHz and signal **D** with $g_{||} \sim 2.37 - 2.39$, $A_{||} = 413 - 434$ MHz, being signal **D** predominant and, in some cases, the only one observed.[50, 52-56] This is the case for the spectrum obtained in this work for the Cu-SAPO-34 prepared by direct synthesis using Cu-TEPA complex and diethyl amine (DEA) as organic structure-directing agents [22], shown in Figure 3c, which consists only of signal **D**.

The differences in the EPR spectra of the three Cu-CHA type materials considered (Cu-SSZ-13, Cu-SSZ-13-int and Cu-SAPO-34) can be due to Cu^{2+} cations placed in different positions. Four different exchange sites have been proposed for Cu^{2+} cations in the CHA-type structure (see Figure 4a). Site **SI**, inside the *d6r* unit, site **SII**, located in the plane of the 6R ring, site **SIII**, in the center of the *cha* cavity, and site **SIV**, at the 8R rings which conform the cavity windows. Divalent Cu^{2+} cations in dehydrated samples tend to firstly occupy position **SII** in 6R rings containing two framework Al atoms (Al pairs), and probably **SI** and/or **SIV** at high Cu loading, while isolated Al can also stabilize $[Cu(OH)]^+$ species close to **SII** or **SIV** sites. [3, 57, 58, 59].

The assignment of the Cu^{2+} EPR signals observed in Cu-SSZ-13 and Cu-SAPO-34 materials to specific species, however, is not clear, often leading to contradictions. [14, 50-56]. In order to clarify the assignment of signals **B** and **C** we have modelled Cu-SSZ-13 and Cu-SAPO-34 with Cu^{2+} located at **SI**, **SII** and **SIV** sites. For that, we have considered the possible distributions of two heteroatoms (Al in the SSZ-13 zeolite and Si in the AlPO-34) generating the framework negative charge in the *d6r* unit, and the fact that Cu^{2+} can bind stronger to some O_f atoms. The computational simulations led to the models depicted in Figure 5, and the EPR parameters summarized in Table 2.

For modeling Cu^{2+} in a **SI** site, two Al atoms in SSZ-13 or two Si atoms in SAPO-34

were located in opposite positions of the *d6r* unit, i.e. one in each 6-membered rings, giving rise to the so-called D6R model. However, in our periodic calculations for Cu-SSZ-13, Cu^{2+} in site **SI** (inside the *d6r*) was found to be unstable as it was always shifted to the center of the 6-ring upon optimization (model D6R for **SII** site, structure **6** in Figure 5), while both **SI** and **SII** sites in a D6R model could be obtained for Cu-SAPO-34 (structures **12** and **13** in Figure 5). To simulate Cu^{2+} at a **SII** site in the Cu-SSZ-13 zeolite, the two Al atoms were located in the same 6R either separated by a –O-Si-O-Si-O– chain in opposite positions or separated by one –O-Si-O– unit, giving rise to the models denoted here as 6R-A and 6R-B, respectively. Notice that, for SAPO-34, 6R-A disposition is not possible. Moreover, Cu^{2+} cation in a 6R can either bind four oxygen atoms adjacent to the two heteroatoms (6R-A1, 6R-B1) or bind three oxygen atoms adjacent to one heteroatom and another oxygen close to the another heteroatom (6R-A2, 6R-B2). Finally, Cu^{2+} at **SIV** (model 8R) was modeled by incorporating two heteroatoms (Al in SSZ-13 or Si in SAPO-34) in the 8R ring (structures **11** and **16** in Figure 5). The corresponding EPR parameters for all these structures are listed in Table 2.

From the results on Cu-SSZ-13, it can be seen that structures D6R, 6R-A2 and 6R-B2, (**6**, **8** and **10** in Figure 5 and Table 2) that share the same coordination geometry, yield similar EPR parameters, although the D6R model provides a smaller $A_{||}$ due to the elongation of the forth $Cu-O_f$ bond. The optimized geometry of 6R-A1 system (structure **7**) is much more similar to a square planar Cu^{2+} complex and accordingly its parameters change toward smaller values of $g_{||}$ and larger values of $A_{||}$, while the opposite trend is observed for 6R-B1 (structure **9**), as the system gets farther away from a square planar-like geometry. Thus, it is not the framework position of the Al atoms alone what produces significant changes in the EPR parameters, but also the Cu^{2+} coordination to different oxygen atoms of the 6R ring.

Among the structures reported on Table 2, 6R-A2 and 6R-B2 (structures **8** and **10** in Figure 5 and Table 2) provide excellent agreement with signal **C**, whereas D6R and 6R-B1 models (structures **6** and **9**) show too low $A_{||}$ values. On the other hand, the 8R structure has both EPR parameters too low for either **C** or **D** signals, in agreement with the previous statements on the preferential positions of Cu^{2+} at **SII** sites.

However, it is clear that no structure in Figure 5 is able to account for signal **D**. Given that the spectroscopic parameters of signal **D** are close to those of an octahedral structure

-note in fact how similar they are to those of **A** and **B** signals -, higher coordination structures were modelled. Site **SI** is an immediate candidate but, as mentioned above, in Cu-SSZ-13 Cu^{2+} always moved to the center of the 6-ring upon optimization. Thus, we explored the possibility of increasing the coordination of Cu^{2+} by interaction with hydroxyls or water molecules surviving the dehydration procedure. Therefore we modelled both the addition of a OH^- species in Cu-SSZ-13 zeolite systems with 1 or 2 Al atoms, and the addition of one to three water molecules to produce higher coordination structures, as signals similar to **D** have also been assigned to $[Cu(H_2O)_3(O_f)_3]^{2+}$ species in other zeolites. [48, 56] In order to model the $[Cu^{2+}(OH^-)]^+$ species in systems containing two Al atoms, a proton (H^+) was used to compensate the second charge, located in a O_f atom bonded to the farthest Al atom. For the sake of clarity, only the results for the 6R-B2 and 8R models are shown in Figure 6, with the corresponding EPR parameters in Table 3, whereas the structures and parameters for the remaining systems can be found in Figure S3 and Table S4.

For $[Cu(OH)]^+$ species in Cu-SSZ-13 models, a trigonal planar structure is obtained in almost all cases regardless of the number of Al atoms or their position in the framework (structures **17-19**), with the Cu^{2+} slightly shifted toward the *cha* cavity binding the hydroxyl and the two oxygen atoms closest to an Al. In some cases, however, the Cu^{2+} cation stays in the 6R ring binding two oxygens close to different Al atoms and a third one next to Si atoms at a longer bond distance (structure **20**) producing rhombic symmetry signals. Nevertheless, the calculated parameters of all of these $[Cu(OH)]^+$ species are too low to be assigned to signal **D**.

Upon the addition of just one water molecule to Cu^{2+} in 6R rings, the Cu^{2+} cation can either stay in the 6R ring producing 5-coordinated structures of almost square pyramid geometry (structures **21** and **23**), or the water can break one of the four $Cu-O_f$ bonds by interacting through hydrogen bonds, producing in this case a 4-coordinated square planar-like structure (structure **22**). This latter structure shows spectroscopic parameters characteristic of square planar geometry, whereas the 5-coordinated Cu^{2+} cations provide much larger values of $g_{||}$ and lower values of $A_{||}$. Indeed, the EPR parameters obtained for structures **21** and **23** with Cu^{2+} in square pyramidal geometry are fully consistent with signal **D**. In 8R frameworks, given the more space available, only the square planar-like coordination is obtained (structure **29**).

The adsorption of a second water molecule on Cu-SSZ-13 produces 4- or 5-coordinated structures, again depending on whether another Cu-O_f bond is broken or not. This time, however, the 5-coordinated structures deviate more from square pyramid geometries, and rhombic species of lower g_z are obtained for structures **24** and **25**. Finally, for $[Cu(H_2O)_3(O_f)_3]^{2+}$ species, the water molecules added interact with oxygen atoms of the zeolite framework through hydrogen bonds, hence producing structures that deviate from the octahedral geometries expected. The distortion is greater in the S**II** site, and as a result somewhat rhombic parameters are obtained for structure **27** and **28** whereas those of structure **30** remain axial. In addition, often one of the Cu-O_f bonds is elongated, and thus the calculated $g_{||}$ values are lower, more characteristic of a 5-coordinated structure (structures **27, 28, 30**).

In summary, for Cu-SSZ-13 we can assign signal **C** to isolated Cu^{2+} in 6R regardless of the Al atoms distribution, with the ion binding to three O_f atoms near one of the Al atoms and to a fourth O_f that is opposite, whereas signal **D** can be explained through partially hydrated S**II** sites, i.e. square pyramid $[Cu(H_2O)(O_f)_4]^{2+}$-species (see Table 4). Moreover, these $[Cu(H_2O)(O_f)_4]^{2+}$ structures providing parameters assignable to **D** are obtained only from 6R-B2 and 6R-A2 Al distributions (see also Structure **S18** in Figure S3 and Table S4), which also provided the best agreement with signal **C**. Therefore, these computational results point to 6R-B2 and 6R-A2, where Cu^{2+} is coordinated to three O_f close to one Al atom and a fourth O_f close to the another Al, as the predominant Cu^{2+} sites in Cu-SSZ-13.

Regarding Cu-SAPO-34, from the results on Table 2 we find again that the 8R structure has $g_{||}$ and $A_{||}$ EPR parameters too low for either signal **C** or **D**. Similarly, S**II** structures provide in general good agreement with signal **C**. However, in this case the structures D6R and 6R-B2, (**13** and **15** in Table 2 and Figure 5) which apparently share the same coordination structure, are the ones that yield more different parameters. A close inspection of the structures reveals that while the structures discussed for Cu-SSZ-13 have nearly the same bond distances, in Cu-SAPO-34 the fourth Cu-O_f bond in structure **15** is significantly shorter, producing a much more square planar structure that is reflected in its lower $g_{||}$ parameter (see Figure S4 and Table S5 for details). Thus, for Cu-SAPO-34 we find that D6R and 6R-B1 structures (**13** and **14**) provide the best agreement with **C**.

With respect to the S**I** site, we found again that Cu^{2+} in such position moves upon

optimization in contradiction with previous studies by Uzunova et al. [61] reporting **SI** (within the *d6r* unit) as the most stable site for Cu^{2+} in Cu-SAPO-34 when using a small cluster model to simulate the catalyst. A significantly less stable structure (+1.4 eV) where the ion is inside the *d6r* unit can nevertheless be obtained (structure **12**), and its rhombic EPR parameters are displaced indeed towards those of signal **D**, i.e, larger $g_{||}$ and lower $A_{||}$. The structure can be further modelled and fixed so that parameters characteristic of signal **D** are obtained (structure **32** in Figure 7 and Table 4), but, as mentioned, such structure is not stable at our computational level.

Therefore, we followed the same reasoning as before and explored the possibility of having hydrated species also in Cu-SAPO-34. In general, the same trigonal planar structures are obtained for $[Cu(OH)]^+$ species and the same 4-, 5- and 6-coordinated structures for $[Cu(H_2O)_n(O_f)_m]^{2+}$ species, with calculated spectroscopic parameters similar to those of Cu-SSZ-13. Due to this, only the structures assignable to signal **D** are shown in Figure 7, with their parameters specified in the summary of Table 4. The remaining structures and their calculated parameters can be consulted in Figure S3 and Table S4 of the Supporting Information.

Interestingly, we find again that the $[Cu(H_2O)(O_f)_4]^{2+}$ species obtained by binding one water molecule to Cu^{2+} in the two **SII** sites responsible for signal **C** (structures **33** and **34**) provide the best agreement with signal **D**. The octahedral $[Cu(H_2O)_3(O_f)_3]^{2+}$ at **SIV** site in this case retains the third $Cu-O_f$ bond that was elongated in structure **30**, thus providing a higher value of $g_{||}$, but it is still not close enough to that of signal **D**.

To sum up, we can conclude that in both dehydrated Cu-SSZ-13 and Cu-SAPO-34 materials isolated Cu^{2+} ions are located at the 6R rings of the *cha* cage, i.e. at **SII** sites, coordinated to four O_f, producing signal **C**, whereas square pyramid-like structures arising from the adsorption of one water molecule in the same **SII** sites can account for signal **D**. For this latter signal, however, the **SI** site remains being also a possibility for Cu-SAPO-34. Additionally, the two materials show different preferential Cu^{2+} positions, with structures 6R-A2 and 6R-B2 for Cu-SSZ-13 and structures D6R and 6R-B1 for Cu-SAPO-34 providing the best agreement with experimental data.

Finally, we noticed that in a recent study by Godiksen et al.[14] three signals slightly different to the more common **C** or **D** are observed for Cu-SSZ-13, further showing the wide variability on the final EPR spectra depending on many parameters. Their first

signal, with $g_{||} = 2.325$ and $A_{||} = 487$, has previously been reported and assigned to Cu/Al_2O_3 species presumably produced in the dehydration process, [52] although several of our structures with different Al distribution and 1-3 water molecules attached also show EPR parameters reasonably similar to this signal (structures **S12, S16, S23, S27** and **S32** in Figure S3 and Table S4), as well as isolated Cu^{2+} in our 6R-A1 model where it is in square planar coordination (structure **7** in Figure 5 and Table 2). Moreover, adding a water molecule to this structure produces others whose calculated parameters are very similar to those of the second signal reported by Godiksen et al., with $g_{||} = 2.358$, $A_{||} = 464$ (structures **S10** and **S17** in Figure S3 and Table S4). In addition, although the $A_{||}$ value of 6R-B1 system (structure **9** in Figure 5 and Table 2) seems a bit off, its $g_{||}$ value is closer to that of this signal, suggesting perhaps a contribution from this structure. We did not obtain, however, structures with such high values of both parameters as Godiksen et al. obtained for their third signal with $g_{||} = 2.388$, $A_{||} = 530$. Given its low intensity and the parameters discussed in the hydrated section, they may be due to some octahedral $[Cu(H_2O)_6]^{2+}$ or $[Cu(H_2O)_5]^{2+}$ complexes surviving the dehydration process, as the authors themselves propose a 5-coordination structure.

Dehydrated Cu-ZSM-5

Figure 3d shows the EPR spectrum of Cu-ZSM-5 after dehydration at 450ºC, which presents two signals labelled **E** and **F**. All previous experimental studies report the same two signals, with values of $g_{||} = 2.32 – 2.34$ and $A_{||} = 463 – 500$ for **E** and $g_{||} = 2.27 – 2.29$ and $A_{||} = 546 – 576$ for **F**. Signal **F** is assigned to a square planar coordination, and **E** is consequently described as square pyramidal due to its higher $g_{||}$ and lower $A_{||}$ with respect to **F** [61-64].

Even if the agreement on the different signals observed experimentally is better than for the Cu-CHA catalyst, the MFI structure of zeolite ZSM-5 is more complicated, as there are up to four different rings, labeled α, β, γ and δ (see Figure 4b) which could allocate the Cu^{2+} site, each having also several possible Al relative dispositions. The issue about whether there are 1 or 2 Al per ring in the structure has been the subject of some studies [65], but there is not a consensus as to the distribution, other than it is not random. Computational studies on the stability of the relative distributions, on the other hand, concluded that there are no energetically significantly preferential sites for the Al atoms [17, 66]. Indeed, the structure provides so many energetically similar possibilities that it

is probable that many different sites within the material produce similar environments for the Cu^{2+} and contribute to the signals observed [15].Groothaert et al. [17] calculated the EPR parameters of several structures with Cu^{2+} in the α, β and γ 6-rings and δ 5-ring, including different dispositions for 1 and 2 Al atoms, finding that most structures provided $g_∥$ values that agree with either **E** or **F**. Taking into account that from experimental EPR spectra signal **F** appears at higher copper loadings and signal **E** shows higher stability, they concluded that **E** should come from structures in the α-ring with either 1 or 2 Al atoms, in a three, four of five-fold coordination, and **F** from structures with 1 Al in four-fold coordination in the rest of the rings. However, Witcherlová et al. [67] suggested that square pyramidal complexes were more probable in β and γ sites, whereas the α-ring would provide square planar geometries, and Nachtigallova et al. [66] did obtain square planar geometries for both α and γ rings in their calculations. Given that Grootheart et al. [17] used and optimized a cluster model, there is room for questioning whether the optimized geometries are representative of the material. In order to shed some light into this, we optimized a periodic model of Cu-ZSM-5 structures with the Cu^{2+} ion located at the three different 6-ring sites α, β and γ in the different possible distributions for the 2 Al atoms. The crystallographic T positions where the Al atoms are incorporated in are specified for each structure in Figure 8 and also in parenthesis in Tables 5-6. α and β-sites are 6-ring structures in which the six T-sites are unequivalent, whereas the γ-site has three pairs of equivalent T-sites due to a symmetry plane. Besides, α and γ sites have an additional O-T-O or O-T-O-T-O bridge, respectively. Also, structures with two Al substitutions leaving just one Si atom between them have been reported as more unstable [66], and thus these possibilities were only modelled for some structures as reference (**38** and **47**). Finally, other 2 Al distributions were added in which the second Al atom is not in the 6-ring of the site, to account for situations where the copper ion is close to 1 Al atom only (structures **39, 43-44, 48-49**).

For almost all systems in Figure 8 we obtained 4-coordinated structures of distorted square planar geometries, being structures **42**, **43** and **44** the only ones with five-fold coordination. In 4-coordinated structures the Cu^{2+} cation binds to four O_f in similar ways to those described for the Cu-SSZ-13 catalyst, namely, with four more equivalently spread Cu-O_f bonds (structures **35, 40, 41, 45, 48**) or with three Cu-O_f bonds closer to one side and a fourth Cu-O_f bond with an opposite oxygen (structures **36-39, 46-47, 49**). As a matter of fact, the calculated parameters of the structures of the first group show lower

values of $g_{||}$ and higher values of $A_{||}$ than the rest, thus being assignable to signal **F** (see Table 5). This type of structures seem to be favored in systems where the 2 Al atoms are placed on opposite T-sites of the 6-ring but lie very close to each other due to the ellipsoidal shape of the β rings in ZSM-5. Among them, the β(4,10), γ(11,11) and α(1,7) structures, (**40**, **45** and **35**) are the most stable of all the Cu-ZSM-5 structures modelled, in agreement with previous studies [17, 66]. However, since signal **F** has lower stability and is a secondary site at lower coverages, Groothaert et al. discussed the possibility of said most stable structures to be actually inexistent in the real catalyst as a consequence of the corresponding T-sites being too close to be occupied by Al simultaneously. Regarding the remaining systems, with the exception of structures **38-39** and **43**, that give too low values of $A_{||}$, the rest provide spectroscopic parameters that show larger values of $g_{||}$ and lower values of $A_{||}$, in agreement with signal **E**. Among them, as mentioned, only structures **42, 43** and **44** are 5-coordinated structures, all showing a square-pyramid geometry and corresponding to β sites, in agreement with Witcherlová et al. and with the square planar structures for α and γ sites of Nachtigallova et al. Interestingly, structures **43** and **44** were obtained when each Al atom was in a different β 6-ring, in opposite positions, forming a structure analogous to the D6R model discussed for the CHA catalysts. However, as explained before, the more ellipsoidal shape of the β 6-ring in MFI provides a smaller separation of the two Al atoms as compared with the distance they are at within the *d6r* cage of CHA, and as a result the copper ion can indeed be stabilized through the interaction with more framework oxygen atoms, hence producing higher coordination structures. This type of structures are also in agreement with the higher stability experimentally observed for signal **E**, as the access to the Cu^{2+} ion is more difficult.

In summary, we observe a distribution of structures from all 6-ring sites contributing to each signal of Cu-ZSM-5, with mainly 4-coordinated square-planar-like structures of more spread $Cu-O_f$ bonds accounting for signal **F** whereas other 4-coordinated and square-pyramid–like 5-coordinated structures can contribute to signal **E**. Among them, the structures that provide the best agreement with signals **E** and **F** are summarized in Table 6.

3.3. Interaction of Cu-CHA catalysts with reactants

In a second step we studied the interaction of Cu-SSZ-13 and Cu-SAPO-34 catalysts with

the reactant molecules involved in the NH$_3$-SCR-NOx reaction, that is, NH$_3$, NO, and a mixture of NO+O$_2$.

NH$_3$ adsorption

Figure 9 shows the EPR spectra of the two catalysts after the addition of NH$_3$ in excess (6 equivalents of NH$_3$ per Cu) and its evacuation at increasing temperature. The signals obtained for Cu-SSZ-13 (Figure 9a-f) denoted here as **G, H,** and **I** were already described and discussed in a previous work by some of us [68], and were assigned to [Cu(NH$_3$)$_5$]$^{2+}$, [Cu(NH$_3$)$_2$(O$_f$)$_2$]$^{2+}$ and [Cu(NH$_3$)(O$_f$)$_3$]$^{2+}$ complexes, respectively. As explained in that work, upon NH$_3$ addition [Cu(NH$_3$)$_5$]$^{2+}$ complexes are formed and stabilized in the zeolites through hydrogen bonds near the 6-ring sites, producing signal **G**, while the remaining complexes are progressively formed and detected with subsequent desorption of NH$_3$ molecules during the evacuation. The **H** band associated to [Cu(NH$_3$)$_2$(O$_f$)$_2$]$^{2+}$ in Cu-SSZ-13 is not observed in the spectrum of Cu-SAPO-34 and instead, an additional signal **J** appears midway through evacuation. Therefore, we modelled the adsorption of 1-3 NH$_3$ molecules in the Cu-SSZ-13 and Cu-SAPO-34 catalysts, along with the square pyramid [Cu(NH$_3$)$_5$]$^{2+}$ and square planar [Cu(NH$_3$)$_4$]$^{2+}$ complexes. The optimized structures are shown in Figure 10, with the corresponding EPR parameters in Table 7.

Upon the addition of just one ammonia molecule, the Cu^{2+} cation is always moved from its position at the 6R ring, as the interaction with the molecule breaks one of the four Cu-O$_f$ bonds. Thus, contrary to the situation with water, no 5-coordinated structures are obtained, and consequently the calculated parameters show lower values of $g_{||}$ characteristic of a 4-coordinated structure. In structure **52** the NH$_3$ molecule interacts with two framework oxygen atoms of the 6R ring through hydrogen bonds, and a shortening of one of the three close Cu-O$_f$ bonds is produced, resulting in a more square planar structure that shows a further lower value of $g_{||}$. This structure provides the best agreement with the corresponding signal **I** (see Table 7). The same type of structures and parameters are obtained for Cu-SSZ-13, with the 6R-B distribution in structure **64** yielding EPR parameters matching signal **I**.

The adsorption of a second molecule always produces the breaking of another Cu-O$_f$ bond and the formation of a 4-coordinated structure that moves the Cu^{2+} cation further away from the ring. The calculated parameters show correspondingly similar values, with lower values of $g_{||}$ and higher values of $A_{||}$ in agreement with the experimental change observed

19

from signal **I** to signal **H** in Cu-SSZ-13 and to signal **J** in Cu-SAPO-34. As shown in Table 7, there is a noticeable difference in the hyperfine parameters obtained for Cu-SSZ-13 and Cu-SAPO-34, being a bit lower for the former. Nevertheless, both materials follow the trend described, in this case with no significantly different parameters when different Al (or Si) distributions are considered. The values obtained from the computational simulation agree with the previous assignment of signal **H** to $[Cu(NH_3)_2(O_f)_2]^{2+}$ species.

Addition of a third molecule produces several different environments for Cu^{2+} in both catalysts. In structures **56** and **68**, besides being coordinated to three NH_3 molecules, the Cu^{2+} cation is still directly attached to one framework O_f atom, with weaker axial interactions with another two O_f, and the calculated $g_{||}$ and $A_{||}$ values are not too different from those obtained for $[Cu(NH_3)_2(O_f)_2]^{2+}$ systems. In 4-coordinated structures like **59**, **71** and **73**, that only keep one $Cu-O_f$ bond, the Cu^{2+} is much more displaced towards the *cha* cavity hence losing the axial interaction and producing low values of $g_{||}$, closing in to that of $[Cu(NH_3)_4]^{2+}$. Structures **58, 70** and **72** correspond to intermediate situations to the previous two. Finally, structure **57** retains two $Cu-O_f$ bonds and shows a distorted five-fold coordination of higher $g_{||}$, whereas in structure **69**, which only preserves one $Cu-O_f$, the similarly higher $g_{||}$ is due to the tetragonal distortion produced by the bending of the species to stablish hydrogen bonds. Altogether, signal **J** observed in Cu-SAPO-34 could be assigned to a $[Cu(NH_3)_3(O_f)_n]^{2+}$ system showing a distorted five- or six-fold coordination or to a square planar $[Cu(NH_3)_4]^{2+}$ complex interacting with the zeolite framework, which actually provides the best agreement in our study (see Table 8).

All in all, our computational calculations reproduce the experimental trends observed, as can be seen in the summary of Table 8. Furthermore, the data presented here point to 6R-B as the predominant location of Al or Si atoms in Cu-SSZ-13 and Cu-SAPO-34, respectively, which is fully consistent with the results obtained for the dehydrated catalysts.

NO adsorption

The addition of NO at low temperature (-170 ºC) produces EPR spectra of very low intensity in Cu-SSZ-13 and Cu-SAPO-34 materials, due to the formation of diamagnetic and thus undetectable Cu^{2+}-NO species (see Figure 11). There is, however, a weak and practically isotropic signal **M** in both catalysts, which has been assigned to a Cu^+-NO complex that is only stable at such temperatures [69-71] and has already been seen in

other zeolites after a similar NO adsorption [72]. The appearance of this band in the spectra indicates, therefore, the presence of Cu^+ in both samples.

The adsorption of one NO molecule on a Cu^+ cation produces its displacement towards the *cha* cavity through the formation of a trigonal planar structure similar to that obtained for $[Cu(OH)]^+$ species. The calculated parameters show a very small anisotropy for the Cu^+-NO species, in agreement with some reports [69, 70] which is nevertheless too small to be detected in spectra of such low intensity. Thus, we compare this time the isotropic values of both spectroscopic parameters, i.e. g_{iso} and A_{iso}, in all models (Figure 12, Table 9). The parameters of isotropic species are generally more accurately calculated and, as a matter of fact, the computed parameters for all the Cu^+-NO structures are very similar and in very good agreement with the experimental data, regardless of the material and distribution considered.

Adsorption of a NO/O$_2$ mixture

Figure 13 shows the EPR spectra of both Cu-SSZ-13 and Cu-SAPO-34 catalysts in the presence of NO and O_2 measured at different temperatures (-170 ºC, 25 ºC and 230 ºC). Spectra at -170 ºC in the presence of O_2 show a wide unstructured signal due to the interaction of Cu^{2+} with liquid oxygen, which is produced at such temperature within the pores of the material due to pressure [73,74]. At higher temperatures, the same signal **N** can be seen for both catalysts at 25 ºC and 230 ºC, and it is stable by evacuation up to 300 ºC (see Figure S5).

Such signal was ambiguously assigned in the past to either nitrite or nitrate species formed on Cu^{2+} [75-81], but has been recently attributed to $[Cu^{2+}NO_3^-]^+$ [15, 82] The EPR parameters for nitrite and nitrate structures have been calculated in order to see whether signal **N** could be unequivocally assigned to either of them. The optimized structures can be seen in Figure 14, whereas the parameters are listed in Table 10. Both species preferentially bind to Cu^{2+} through two of their oxygen atoms, thus forming bidentate structures. In such case, two Cu-O_f are broken and the ion is moved again towards the CHA cavity, forming a distorted square planar structure (structures **79-88**). The bidentate structures of nitrate and nitrite species are very similar, hence only somewhat higher values of $g_{||}$ are obtained for the latter. As a result, it is not possible based on this data alone to state unambiguously whether signal **N** is due to formation of a nitrate or a nitrite species.

4. Conclusions

EPR spectroscopy of Cu-SSZ-13, Cu-SAPO-34 and Cu-ZSM-5 catalysts under different conditions combined with molecular modelling of the possible Cu^{2+} structures and their corresponding EPR parameters have allowed the assignment of the paramagnetic signals to specific Cu^{2+} species. The computational methodology employed provides a systematic underestimation of the $g_{\parallel}$ parameters that, being systematic, allows a consistent comparison of trends with the experimental data and an assignment of the EPR signals.

In this work, the main signal **A** observed in the EPR spectra of hydrated Cu-SSZ-13, Cu-SAPO-34 and Cu-ZSM-5 zeolites is attributed to octahedral $[Cu(H_2O)_6]^{2+}$ complexes with C_i or C_1 symmetry, while the presence of a second signal **B** in Cu-SSZ-13 can be associated to the stabilization of a complex similar to the octahedral D_{2h} $[Cu(H_2O)_6]^{2+}$ system.

The two EPR signals **C** and **D** observed in the EPR spectra of dehydrated Cu-SSZ-13 and Cu-SAPO-34 are assigned to Cu^{2+} ions located at **SII** sites in the CHA structure. Isolated Cu^{2+} cations in the plane of the 6-rings of the *d6r* unit are responsible for signal **C**, while square pyramid-like $Cu(H_2O)(O_f)_4$ structures arising from the adsorption of one water molecule in the same **SII** sites can account for signal **D**. In the case of SAPO-34, the possibility of Cu^{2+} at site **SI** inside the *d6r* unit generating signal **D** is not completely discarded.

Two distinct **E** and **F** signals are present in the EPR spectrum of dehydrated Cu-ZSM-5, with a distribution of structures from all 6-ring sites contributing to each signal. It can be concluded that 4-coordinated square-planar-like structures of more spread $Cu-O_f$ bonds mainly account for signal **F** whereas not only square-pyramid 5-coordinated structures but also other 4-coordinated structures can contribute to signal **E**.

The adsorption of NH_3 on Cu-SSZ-13 and Cu-SAPO-34 and its subsequent evacuation at increasing temperature produces four signals **G, H, I** and **J** in the corresponding EPR spectra. The computational modelling agrees with the previous assignment of signals **G** and **I**, present in both catalysts, to $[Cu(NH_3)_5]^{2+}$ and $[Cu(NH_3)(O_f)_3]^{2+}$ complexes, respectively. Signal **H** is only present in the spectrum of Cu-SSZ-13 and is attributed to $[Cu(NH_3)_2(O_f)_2]^{2+}$ species, while signal **J,** only observed in Cu-SAPO-34, could be

assigned to a $[Cu(NH_3)_3(O_f)_n]^{2+}$ system showing a distorted five- or six-fold coordination or to a square planar $[Cu(NH_3)_4]^{2+}$ complex interacting with the zeolite framework.

The computed parameters for the Cu^+-NO structures responsible for the isotropic signal **M** observed after addition of NO to Cu-SSZ-13 and Cu-SAPO-34 catalysts are in very good agreement with the experimental data. Finally, the band **N** appearing in the EPR spectra of Cu-SSZ-13 and Cu-SAPO-34 after addition of a mixture of NO and O_2 is consistent with both nitrite and nitrate species coordinated to Cu^{2+} through two of their oxygen atoms, forming similar bidentate structures in which Cu^{2+} shows a distorted square planar geometry.

The results reported here shed light on the location and geometric environment of Cu^{2+} in Cu-SSZ-13, Cu-SAPO-34 and Cu-ZSM-5 as well as on the nature of the species resulting from the interaction with H_2O, NH_3, NO and NO/O_2. This information can help in the identification of the intermediate species formed during the SCR-NOx reaction using Cu-zeolite catalysis and then on the elucidation of the reaction mechanism. Moreover, the results reported here may help also in in the interpretation of the EPR spectra of Cu-zeolites or Cu-silicoaluminophosphate in general and their interaction with the above mentioned molecules. This is especially valuable given the very few number of studies focused on the interpretation of paramagnetic signals using theoretical modeling.

Acknowledgments

References

[1] Chen H-Y (2014) In: Nova, I., Tronconi, E., (eds.) Urea-SCR Technology for deNOx After Treatment of Diesel Exhausts. Springer, New York.

[2] Brandenberger S, Krocher O, Tissler A, Althoff R (2008) Catal. Rev. Sci. Eng. 50:492-531.

[3] Gao F, Kwak, J, Szanyi J, Peden C H F (2013) Topics in Catal. 56:1441-1459.

[4] Deka U, Lezcano-González, I, Weckhuysen, B. M, Beale, A M (2013) ACS Catal. 3:413-427.

[5] Beale A M, Gao F, Lezcano-Gonzalez I, Peden C H F, Szanyi J (2015) Chem. Soc. Rev. 44:7371-7405.

[6] Zhang R, Liu N, Lei Z, Chen B (2016) Chem. Rev. 116:3658-3721.

[7] Kwak J H, Tonkyn R G, Kim D H, Szanyi J, Peden C H F (2010) J. Catal. 275:187-190.

[8] Bates S A, Verma A, Paolucci C, Parekh A, Anggara T, Schneider W F, Miller J T, Delgass W N, Ribeiro F H (2014) J. Catal. 312:87-97.

[9] Beale A M, Lezcano-Gonzalez I, Slawinksi W A, Wragg D S (2016) Chem. Commun. 52:6170-6173.

[10] Xue J, Wang X, Qi G, Wang J, Shen M, Li W (2013) J. Catal. 297:56-64.

[11] Dedecek J, Kaucky D, Wichterlova B (2000) Microporous and Mesoporous Materials 35-6:483-494.

[12] Mentzen B F, Bergeret G (2007) J. Phys. Chem. C 111:12512-12516.

[13] Gao F, Walter E D, Karp E M, Luo J, Tonkyn R G, Kwak J H, Szanyi J, Peden C H F (2013) J. Catal. 300:20-29.

[14] Godiksen A, Stappen F N, Vennestrom P N R, Giordanino F, Rasmussen S B, Lundegaard L F, Mossin S (2014) J. Phys. Chem. C 118:23126-23138.

[15] Godiksen A, Vennestrom P N R, Rasmussen S, Mossin S (2017) Topics in Catalysis 60:13-29.

[16] Ames W M, Larsen S C (2010) J. Phys. Chem. A 114:589-594.

[17] Groothaert M H, Pierloot K, Delabie A, Schoonheydt R A (2003) Phys. Chem. Chem. Phys. 5:2135-2144.

[18] Delabie A, Pierloot K, Groothaert M H, Weckhuysen B M, Shoonheydt R A (2002) Phys. Chem. Chem. Phys. 4:134-145.

[19] Pierloot K, Delabie A, Groothaert M H, Shoonheydt R A (2001) Phys. Chem. Chem. Phys. 3:2174-2183.

[20] Martinez-Franco R, Moliner M, Thogersen J R, Corma A (2013) ChemCatChem 5:3316-3323.

[21] Moliner M, Franch C, Palomares E, Grill M, Corma A (2012) *Chem. Commun.* 48:8264-8266.

[22] Martínez-Franco R, Moliner M, Concepcion P, Thogersen J R, Corma A (2014) J. Catal. 314:73-82.

[23] Pietrzyk P, Podolska K, Sojka Z (2013) Electron Paramagnetic Resonance 23:264-311.

[24] Malkin E, Repisky M, Komorovsky S, Mach P, Malkina O L, Malkin V G (2011) J. Chem. Phys. 134: 044111-1-044111-8.

[25] Hrobarik P, Repisky M, Komorovsky S, Hrobarikova V, Kaupp M (2011) Theoretical Chemistry Accounts129:715-725.

[26] Gohr S, Hrobarik P, Repisky M, Komorovsky S, Ruud K, Kaupp M (2015) J. Phys. Chem. A 119:12892-12905.

[27] Neese F (2012) The ORCA program system. Wiley Interdisciplinary Reviews: Computational Molecular Science 2:73-78.

[28] Neese F (2005) J. Chem. Phys. 122:034107-1-034107-13.

[29] Neese F (2003) J. Chem. Phys. 118:3939-3948.

[30] Neese F (2001) J. Chem. Phys. 115:11080-11096.

[31] Kossmann S, Kirchner B, Neese F (2007) Molecular Physics 105:2049-2071.

[32] Ames W M, Larsen S C (2009) J. Phys. Chem. A 113:4305-4312.

[33] Neese F (2009) Coordination Chemistry Reviews 253:526-563.

[34] Neese F (2007) Electron Paramagnetic Resonance 20:73-95.

[35] Kresse G, Furthmüller J (1996) Phys. Rev. B 54:11169-11186.

[36] Kresse G, Joubert D (1999) Phys. Rev. B 59:1758-1775.

[37] Perdew J P, Wang Y (1992) Phys. Rev. B 45:13244–13249

[38] Blöchl P (1994) Phys. Rev. B 50:17953-17979.

[39] Becke A D (1993) J. Chem. Phys. 98:5648-5652.

[40] Becke A D (1998) Phys. Rev. A 38:3098-3100.

[41] Lee C T, Yang W T, Parr R G D (1998) Phys. Rev. B 37:785-789.

[42] Heß B A, Marian C M, Wahlgren U, Gropen O (1996) Chem. Phys. Lett. 251:365-371.

[43] Neese F (2003) J. Comput. Chem. 24:1740-1747.

[44] Kutzelnigg W, Fleischer U, Schindler M (1990) In: NMR-Basic Principles and Progress. Springer-Verlag, Heidelberg.

[45] Neese F (2002) Inorganica Chimica Acta 337:181-192.

[46] Sinnecker S, Slep L D, Bill E, Neese F (2005) Inorganic Chemistry 44:2245-2254.

[47] Gao F, Walter E D, Kollar M, Wang Y, Szanyi J, Peden C H F (2014) J. Catal. 319:1-

14.

[48] Conesa J C, Soria J (1979) J. Chem. Soc. Faraday Trans. 75:406-422.

[49] de Almeida K J, Rinkevicius Z, Hugosson H W, Ferreira A C, Agren H (2007) Chemical Physics 332:176-187.

[50] Zamadics M, Kevan L (1992) J. Phys. Chem. 96:8989-8993.

[51] Ma L, Cheng Y S, Cavataio G, McCabe R W, Fu L X, Li J H (2013) Chem. Eng. J. 225:323-330.

[52] Kim Y J, Lee J K, Min K M, Hong S B, Nam I S, Cho B K (2014) J. Catal. *311*:447-457.

[53] Zamadics M, Chen X H, Kevan L (1992) J. Phys. Chem. 96:2652-2657.

[54] Zamadics M, Chen X H, Kevan L (1992) J. Phys. Chem. 96:5488-5491.

[55] Liu X, Wu X, Weng D, Si Z, Ran R (2017) Catalysis Today 281:596-604.

[56] Wang J, Yu T, Wang X Q, Qi G S, Xue J J, Shen M Q, Li W (2012) Appl. Catal. B-Environmental 127:137-147.

[57] Fickel D W, Lobo R (2010) J. Phys. Chem. C 114:1633-1640.

[58] Di Iorio J R, Gounder R (2016) Chem Mater 28:2236-2247.

[59] Paolucci C, Parekh A A, Khurana I, Di Iorio J R, Li H, Albarracin Caballero J D, Shih A J, Anggara T, Delgass W N, Miller J T, Ribeiro F H, Gounder R, Schneider W F (2016) J. Am. Chem.Soc. 138:6028-6048.

[60] Uzunova E L, Mikosch H, Hafner J (2009) Journal of Molecular Structure-Theochem 912:88-94

[61] Kucherov A V, Karge H G, Schlogl R (1998) Microporous and Mesoporous Materials 25:7-14.

[62] Dedecek J, Sobalík Z, Tvaruzkova D, Kaucky D, Wichterlova B (1995) J. Phys. Chem. 99:16327-16337

[63] Kucherov A V, Slinkin A A, Kondrat'ev D A, Bondarenko T N, Rubinstein A M, Minachev Kh M (1985) Zeolites 5:320-324.

[64] Kucherov A V, Gerlock J L, Jen H W, Shelef M (1994) J. Phys. Chem. 98:4892-4894.

[65] Dedecek J, Balgova V, Pashkova V, Klein P, Wichterlova B (2012) Chem. Mat. 24:3231-3239.

[66] Nachtigallova D, Nachtigall P, Sauer J (2001) Phys. Chem. Chem. Phys. 3:1552-1559.

[67] Wichterlova B, Dedecek J, Sobalik Z (1998) In: Treacy M M J, Marcus B K, Bisher

M E, Higgins J B (eds.) Proceedings of the 12th International Zeolite Conference, Materials Research Society, Baltimore, USA, 941–973.

[68] Moreno-Gonzalez M, Hueso B, Boronat M, Blasco T, Corma, A. (2015) J. Phys. Chem. Lett. 6:1011-1017.

[69] Sojka Z, Che M, Giamello E (1997) J. Phys. Chem. B 101:4831-4838.

[70] Prestipino C, Berlier G, Xamena F, Spoto G, Bordiga S, Zecchina A, Palomino G T, Yamamoto T, Lamberti C (2002) Chem. Phys. Lett. 363:389-396.

[71] Umamaheswari V, Hartmann M, Poppl A (2005) J. Phys. Chem. B 109:1537-1546.

[72] Moreno-Gonzalez, M, Palomares A E, Chiesa M, Boronat M, Giamello E, Blasco T (2017) ACS Catalysis 7:3501-3509.

[73] Webb P A, Orr C (1997) Analytical Methods in Fine Particle Technology, Micrometrics.

[74] Yahiro H, Ohmori Y, Shiotani M (2005) Microporous and Mesoporous Materials 83:165-171.

[75] Il'ichev A N, Ukharsky A A, Matyshak V A (1996) Mendeleev Commun. 6:57-59.

[76] Matyshak V A, Il'ichev A N, Ukharsky A A, Korchak V N (1997) J. Catal. 171:245-254.

[77] Kucherov, A V, Gerlock G L, Jen H W, Shelef M (1996) Catalysis Today 27:79-84.

[78] Giamello E, Murphy D, Magnacca G, Morterra C, Shioya Y, Nomura T, Anpo M (1992) J. Catal. 136:510-520.

[79] Lei G D, Adelman B J, Sárkány J, Sachtler W M H (1995) Appl. Catal. B 5:245-256.

[80] Pietrzyk P, Gil B, Sojka Z (2007) Catal. Today 126:103-111.

[81] Konduru M V, Chuang S S C (2000) J. Catal. 196:271-286.

[82] Janssens T V W, Falsig H, Lundegaard L F, Vennestrøm P N R, Rasmussen S B, Moses P G, Giordanino F, Borfecchia E, Lomachenko K A, Lamberti C, Bordiga S, Godiksen A, Mossin S, Beato P (2015) ACS Catal. 5:2832-2845.

Tables

Table 1. Experimental and calculated EPR parameters of the signals indicated in the spectra of Figure 1 (measured at -170°C), and their assignment to specific species. The corresponding DFT optimized structures are depicted in Figure 2.

Exp	Structure	Signal	$g_{\parallel}$	$A_{\parallel}$/MHz	Cu^{2+} species
	All	**A**	*2.391*	*458*	*Cu^{2+} octahedral*
	SSZ-13	**B**	*2.416*	*406*	
DFT	Structure	Symmetry	$g_{\parallel}$	$A_{\parallel}$/MHz	Cu^{2+} species
	1	Oct D_{2h}	2.307[a]	-414[a]	$[Cu(H_2O)_6]^{2+}$
	2	Oct C_i	2.307	-485	$[Cu(H_2O)_6]^{2+}$
	3	Oct C_1	2.273	-494	$[Cu(H_2O)_6]^{2+}$
	4	SqPy	2.258	-515	$[Cu(H_2O)_5]^{2+}$
	5	~SqPl	2.222	-582	$[Cu(H_2O)_4]^{2+}$

[a]Rhombic species, i.e. with three different values in both parameters (g_x, g_y, g_z, A_x, A_y, A_z). The largest components are shown (g_z, A_z).

Table 2. Calculated EPR parameters for the structures in Figure 5.

Catalyst	Structure	Distribution	$g_{\parallel}$	$A_{\parallel}$/MHz	Cu^{2+} site
Cu-.SSZ-13	**6**	D6R	2.243	-368	**SII**
	7	6R-A1	2.226	-539	**SII**
	8	6R-A2	2.243	-484	**SII**
	9	6R-B1	2.255	-383	**SII**
	10	6R-B2	2.242	-492	**SII**
	11	8R	2.194	-203	**SIV**
Cu-SAPO-34	**12**	D6R	2.267[a]	384[a]	**SI**
	13	D6R	2.234	-477	**SII**
	14	6R-B1	2.232	-486	**SII**
	15	6R-B2	2.219	-486	**SII**
	16	8R	2.219	224	**SIV**

[a]Rhombic species. The largest components are shown (g_z, A_z).

Table 3. Calculated EPR parameters for the Cu-SSZ-13 structures in Figure 6.

Structure	Distribution	$g_{\parallel}$	$A_{\parallel}$/MHz	Cu^{2+} species
17	1Al	2.231	-349	$[Cu^{2+}(OH^-)]^+$
18	1Al	2.223	-257	$[Cu^{2+}(OH^-)]^+$
19	6R-B2	2.238	-333	$[Cu^{2+}(OH^-)]^+$
20	6R-B2	2.200^a	-401^a	$[Cu^{2+}(OH^-)]^+$
21	6R-B2	2.282	-419	$CuH_2O(O_f)_4$
22	6R-B2	2.212	-517	$CuH_2O(O_f)_3$
23	6R-B2	2.282	-416	$CuH_2O(O_f)_4$
24	6R-B2	2.257^a	-411^a	$Cu(H_2O)_2(O_f)_3$
25	6R-B2	2.210^a	-406^a	$Cu(H_2O)_2(O_f)_3$
26	6R-B2	2.207	-528	$Cu(H_2O)_2(O_f)_2$
27	6R-B2	2.219^a	-489^a	$Cu(H_2O)_3(O_f)_3$
28	6R-B2	2.224^a	-545^a	$Cu(H_2O)_3(O_f)_3$
29	8R	2.211	-471	$CuH_2O(O_f)_3$
30	8R	2.235	-512	$Cu(H_2O)_3(O_f)_3$
31	8R	2.246	-528	$Cu(H_2O)_4(O_f)_2$

^{a}Rhombic species. The largest components are shown (g_z, A_z).

Table 4. Experimental and calculated EPR parameters of the signals indicated in the spectra of Figure 4 (measured at -170ºC), and their assignment to specific species. The corresponding DFT optimized structures are depicted in Figure 5.

Exp	Structure	Signal	g_{ll}	A_{ll}/MHz	Cu^{2+} species
	Cu-SSZ-13	**C**	*2.347*	*493*	*Isolated Cu^{2+} at S**II***
	Cu-SAPO-34	**D**	*2.386*	*384*	*Isolated Cu^{2+}*
DFT	Structure	Assignation	g_{ll}	A_{ll}/MHz	Cu^{2+} species
Cu-SSZ-13	**8**	**C**	2.243	-484	6R-A2 S**II**
	10	**C**	2.242	-492	6R-B2 S**II**
	21	**D**	2.282	-419	6R-B2 $CuH_2O(O_f)_4$
	23	**D**	2.282	-416	6R-B2 $CuH_2O(O_f)_4$
	S18[b]	**D**	2.282	-408	6R-A2 $CuH_2O(O_f)_4$
Cu-SAPO-34	**13**	**C**	2.234	-477	D6R S**II**
	14	**C**	2.232	-486	6R-B1 S**II**
	12	**D**	2.267[a]	384[a]	D6R ~S**I**
	32	**D**	2.293	-398	D6R S**I** (not opt)
	33	**D**	2.271	-415	D6R $CuH_2O(O_f)_4$
	34	**D**	2.269	-422	6R-B $CuH_2O(O_f)_4$

[a]Rhombic species. The largest components are shown (g_z, A_z).

[b]See Figure S3.

Table 5. Calculated EPR parameters for the structures in Figure 8.

Structure	Distribution	$g_{\parallel}$	$A_{\parallel}$/MHz	Cu^{2+} site
35	(1,7)	2.200	-563	α
36	(2,11)	2.230	-479	α
37	(5,8)	2.221	-511	α
38	(2,5)	2.219	-369	α
39	(1,1)	2.231	-251	α
40	(4,10)	2.192	-497	β
41	(5,11)	2.186	-547	β
42	(1,7)	2.225	-474	β
43	(1,1)	2.241	-343	β
44	(4,4)	2.231	-459	β
45	(11,11)	2.204	-564	γ
46	(7,12)	2.212	-475	γ
47	(11,12)	2.233	-466	γ
48	(10,12)	2.206	-531	γ
49	(10,11)	2.236	-477	γ

Table 6. Experimental and calculated EPR parameters of the signals indicated in the spectra of Figure 4d (measured at -170ºC), and their assignment to specific species. The corresponding DFT optimized structures are depicted in Figure 8.

Exp	Structure	Signal	g_{II}	A_{II}/MHz	Cu^{2+} species
	Cu-ZSM-5	E	*2.323*	*471*	*Cu^{2+} Sq Py*
	Cu-ZSM-5	F	*2.276*	*545*	*Cu^{2+} Sq Pl*
DFT	Structure	Assignation	g_{II}	A_{II}/MHz	Cu^{2+} species
	36	**E**	2.230	-479	α(2,11)
	42	**E**	2.225	-474	β(1,7)
	44	**E**	2.231	-459	β(4,4)
	47	**E**	2.233	-466	γ(11,12)
	49	**E**	2.236	-477	γ(10,11)
	35	**F**	2.200	-563	α(1,7)
	40	**F**	2.192	-497	β(4,10)
	41	**F**	2.186	-547	β(5,11)
	45	**F**	2.204	-564	γ(11,11)
	48	**F**	2.206	-531	γ(10,12)

Table 7. Calculated EPR parameters for the structures in Figure 10.

Distribution	Cu-SAPO-34			Cu-SSZ-13			Cu^{2+} species
	Struc.	g_{ll}	A_{ll}/MHz	Struc.	g_{ll}	A_{ll}/MHz	
D6R	**50**	2.215[a]	377[a]	**62**	2.215	-263	$[Cu(NH_3)_1(O_f)_3]^{2+}$
6R-B/6R-A	**51**	2.219	-444	**63**	2.231	-363	$[Cu(NH_3)_1(O_f)_3]^{2+}$
6R-B	**52**	2.190	-466	**64**	2.199	-452	$[Cu(NH_3)_1(O_f)_3]^{2+}$
D6R	**53**	2.171	-539	**65**	2.185	-470	$[Cu(NH_3)_2(O_f)_2]^{2+}$
6R-B/6R-A	**54**	2.171	-554	**66**	2.179	-495	$[Cu(NH_3)_2(O_f)_2]^{2+}$
6R-B	**55**	2.175	-528	**67**	2.175	-489	$[Cu(NH_3)_2(O_f)_3]^{2+}$
D6R	**56**	2.173	-562	**68**	2.179	-520	$[Cu(NH_3)_3(O_f)_3]^{2+}$
6R-B/6R-A	**57**	2.205	-492	**69**	2.218	-440	$[Cu(NH_3)_3(O_f)_2]^{2+}$
6R-B	**58**	2.159	-569	**70**	2.168	-548	$[Cu(NH_3)_3(O_f)_3]^{2+}$
D6R	**59**	2.154	-472	**71**	2.140	-498	$[Cu(NH_3)_3(O_f)_1]^{2+}$
6R-A				**72**	2.164	-576	$[Cu(NH_3)_3(O_f)_2]^{2+}$
6R-B				**73**	2.155	-469	$[Cu(NH_3)_3(O_f)_1]^{2+}$
-	**60**	2.137	-600				$[Cu(NH_3)_4]^{2+}$
-	**61**	2.161	-543				$[Cu(NH_3)_5]^{2+}$

[a]Rhombic species. The largest components are shown (g_z, A_z).

Table 8. Experimental and calculated EPR parameters of the signals indicated in the spectra of Figure 9 (measured at -170°C), and their assignment to specific species. The corresponding DFT optimized structures are depicted in Figure 10.

Exp	Structure	Signal	g_{II}	A_{II}/MHz	Cu^{2+} species
	Both	**I**	*2.297*	*437*	$[Cu(NH_3)_1(O_f)_3]^{2+}$
	Cu-SSZ-13	**H**	*2.278*	*539*	$[Cu(NH_3)_2(O_f)_2]^{2+}$
	Cu-SAPO-34	**J**	*2.231*	*575*	-
	Both	**G**	*2.246*	*503*	$[Cu(NH_3)_5]^{2+}$
DFT	**Structure**	**Assignation**	g_{II}	A_{II}/MHz	Cu^{2+} species
Cu-SAPO-34	**52**	**I**	2.190	-466	6R-B $[Cu(NH_3)_1(O_f)_3]^{2+}$
Cu-SSZ-13	**64**	**I**	2.199	-452	6R-B $[Cu(NH_3)_1(O_f)_3]^{2+}$
Cu-SSZ-13	**65**	**H**	2.185	-470	D6R $[Cu(NH_3)_2(O_f)_2]^{2+}$
Cu-SSZ-13	**66**	**H**	2.179	-495	6R-B $[Cu(NH_3)_2(O_f)_2]^{2+}$
Cu-SSZ-13	**67**	**H**	2.175	-489	6R-B $[Cu(NH_3)_2(O_f)_3]^{2+}$
Cu-SAPO-34	**58**	**J**	2.159	-569	6R-B $[Cu(NH_3)_3(O_f)_3]^{2+}$
	60	**J**	2.137	-600	$[Cu(NH_3)_4]^{2+}$
	61	**G**	2.161	-543	$[Cu(NH_3)_5]^{2+}$

Table 9. Experimental and calculated EPR parameters of the signals indicated in the spectra of Figure 11 and their assignment to specific species. The corresponding DFT optimized structures are depicted in Figure 12.

Exp	Structure	Signal	g_{iso}	A_{iso}/MHz	Cu^{2+} species
	Cu-SSZ-13	**M**	*1.991*	*507*	*Cu^+NO*
DFT	**Structure**	**Assignation**	g_{iso}	A_{iso}/MHz	Cu^{2+} species
Cu-SSZ-13	**74**	**M**	1.980	460	D6R $[CuNO]^+$
	75	**M**	1.982	519	6R-A $[CuNO]^+$
	76	**M**	1.981	500	6R-B $[CuNO]^+$
Cu-SAPO-34	**77**	**M**	1.981	498	D6R $[CuNO]^+$
	78	**M**	1.979	474	6R-B $[CuNO]^+$

Table 10. Experimental and calculated EPR parameters of the signals indicated in the spectra of Figure 13 and their assignment to specific species. The corresponding DFT optimized structures are depicted in Figure 14.

Exp	Structure	Signal	$g_{\parallel}$	$A_{\parallel}$/MHz	Cu^{2+} species
	Cu-SSZ-13	N	*2.287*	*535*	*$[Cu^{2+}NO_x^-]^+$*
DFT	**Structure**	**Assignation**	$g_{\parallel}$	$A_{\parallel}$/MHz	Cu^{2+} species
Cu-SSZ-13	**79**	**N**	2.186	-577	D6R $[Cu^{2+}NO_3^-]^+$
	80	**N**	2.188	-573	6R-A $[Cu^{2+}NO_3^-]^+$
	81	**N**	2.188	-570	6R-B $[Cu^{2+}NO_3^-]^+$
Cu-SAPO-34	**82**	**N**	2.180	-584	D6R $[Cu^{2+}NO_3^-]^+$
	83	**N**	2.181	-581	6R-B $[Cu^{2+}NO_3^-]^+$
Cu-SSZ-13	**84**	**N**	2.201	-571	D6R $[Cu^{2+}NO_2^-]^+$
	85	**N**	2.204	-568	6R-A $[Cu^{2+}NO_2^-]^+$
	86	**N**	2.203	-566	6R-B $[Cu^{2+}NO_2^-]^+$
Cu-SAPO-34	**87**	**N**	2.195	-577	D6R $[Cu^{2+}NO_2^-]^+$
	88	**N**	2.197	-575	6R-B $[Cu^{2+}NO_2^-]^+$

Figures

A: $g_\parallel = 2.391$ $A_\parallel = 458$ MHz
B: $g_\parallel = 2.416$ $A_\parallel = 406$ MHz
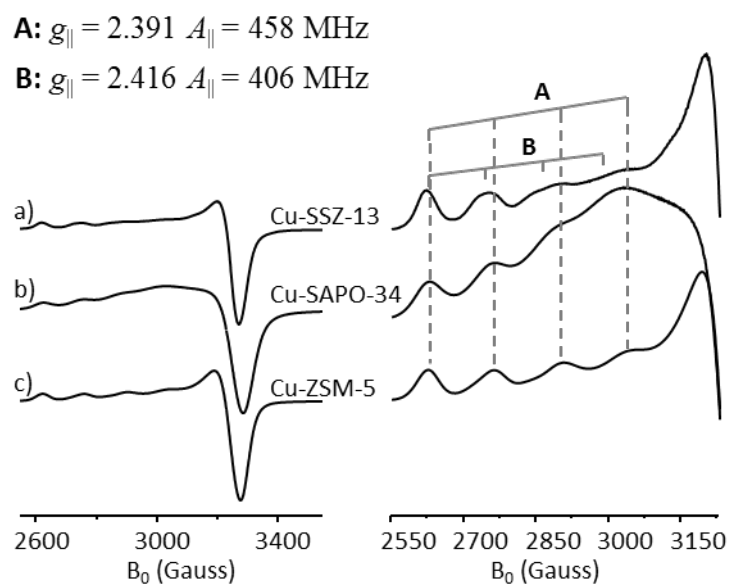
Figure 1. EPR spectra (left) and magnification of the low-field hyperfine structure (right) of hydrated Cu-SSZ-13, Cu-SAPO-34 and Cu-ZSM-5 recorded at -270ºC.
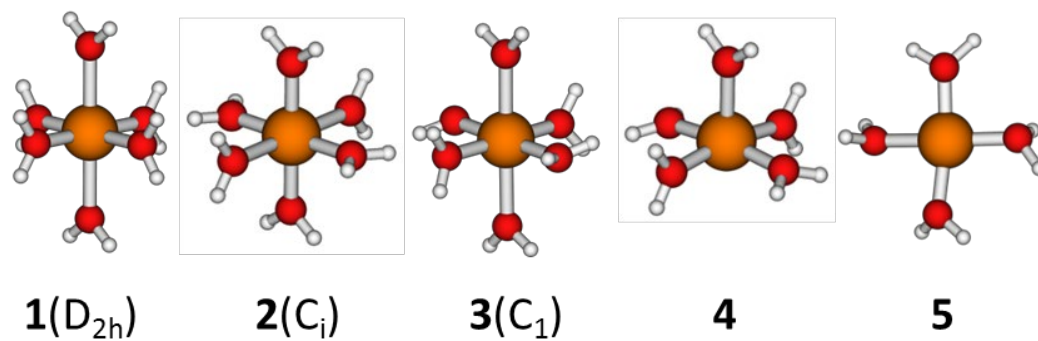
Figure 2. Optimized structures of $[Cu(H_2O)_n]^{2+}$ complexes.

C: $g_\parallel = 2.347$ $A_\parallel = 493$ MHz   E: $g_\parallel = 2.323$ $A_\parallel = 471$ MHz

D: $g_\parallel = 2.386$ $A_\parallel = 384$ MHz   F: $g_\parallel = 2.276$ $A_\parallel = 545$ MHz
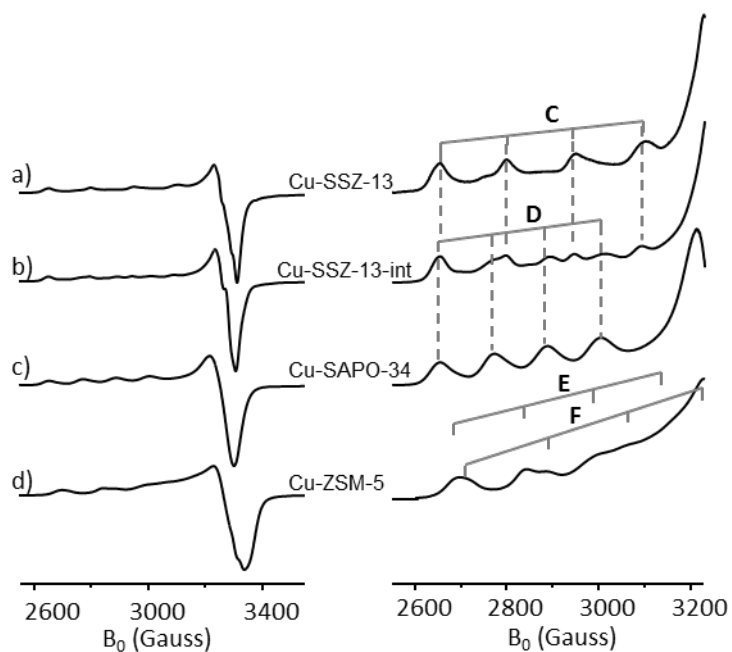
Figure 3. EPR spectra (left) and magnification of the low-field hyperfine structure (right) of a) Cu-SSZ-13, b) Cu-SSZ-13-int, c) Cu-SAPO-34 and d) Cu-ZSM-5 recorded at -170ºC after dehydration at 450ºC.
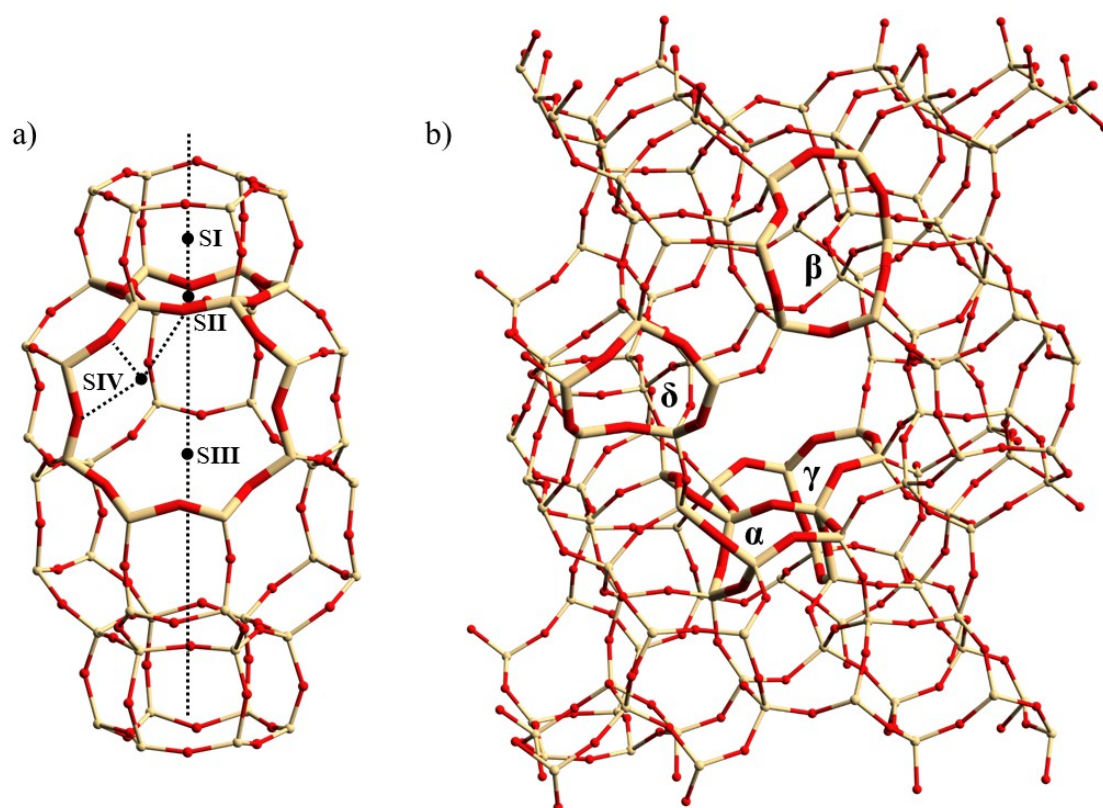
Figure 4. Possible exchange sites for Cu^{2+} cations in a) CHA and b) MFI zeolite structures.
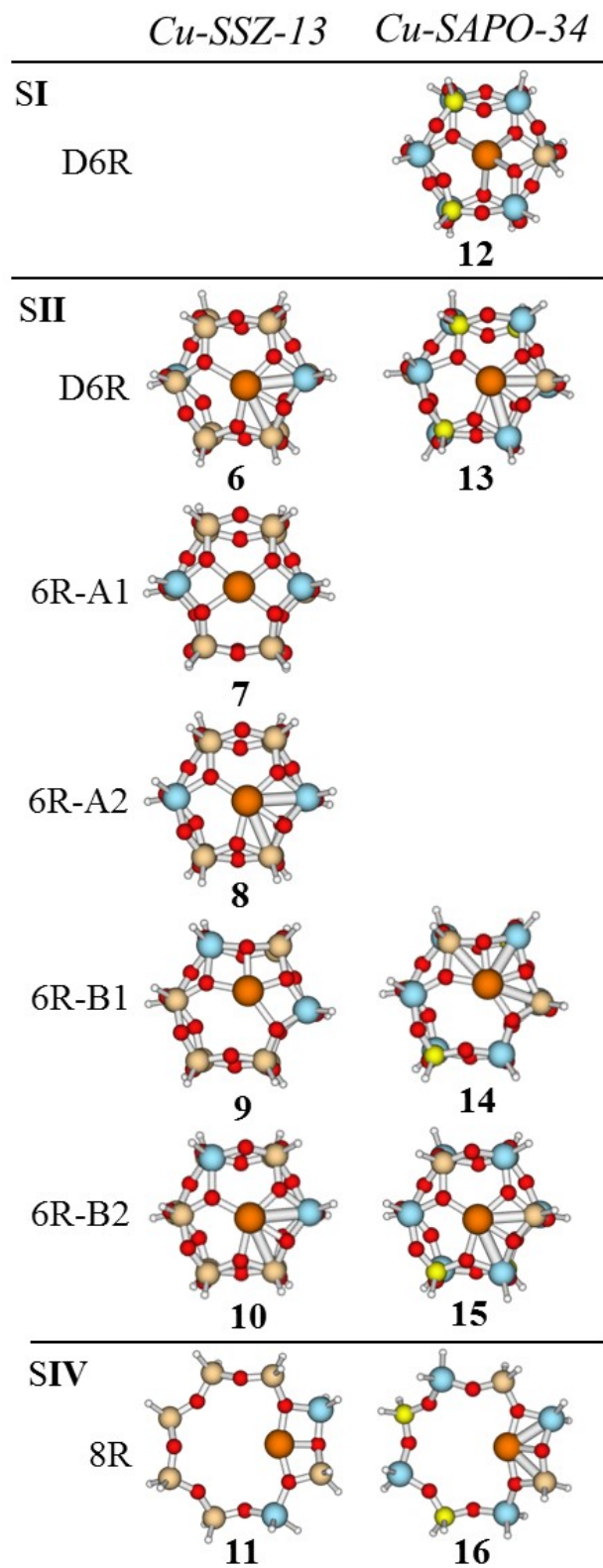
Figure 5. Optimized structures of dehydrated Cu-SSZ-13 and Cu-SAPO-34 with different Al and Si distributions. Si, Al, P, O, Cu and H atoms are depicted in sand, blue, yellow, red, orange and white, respectively.
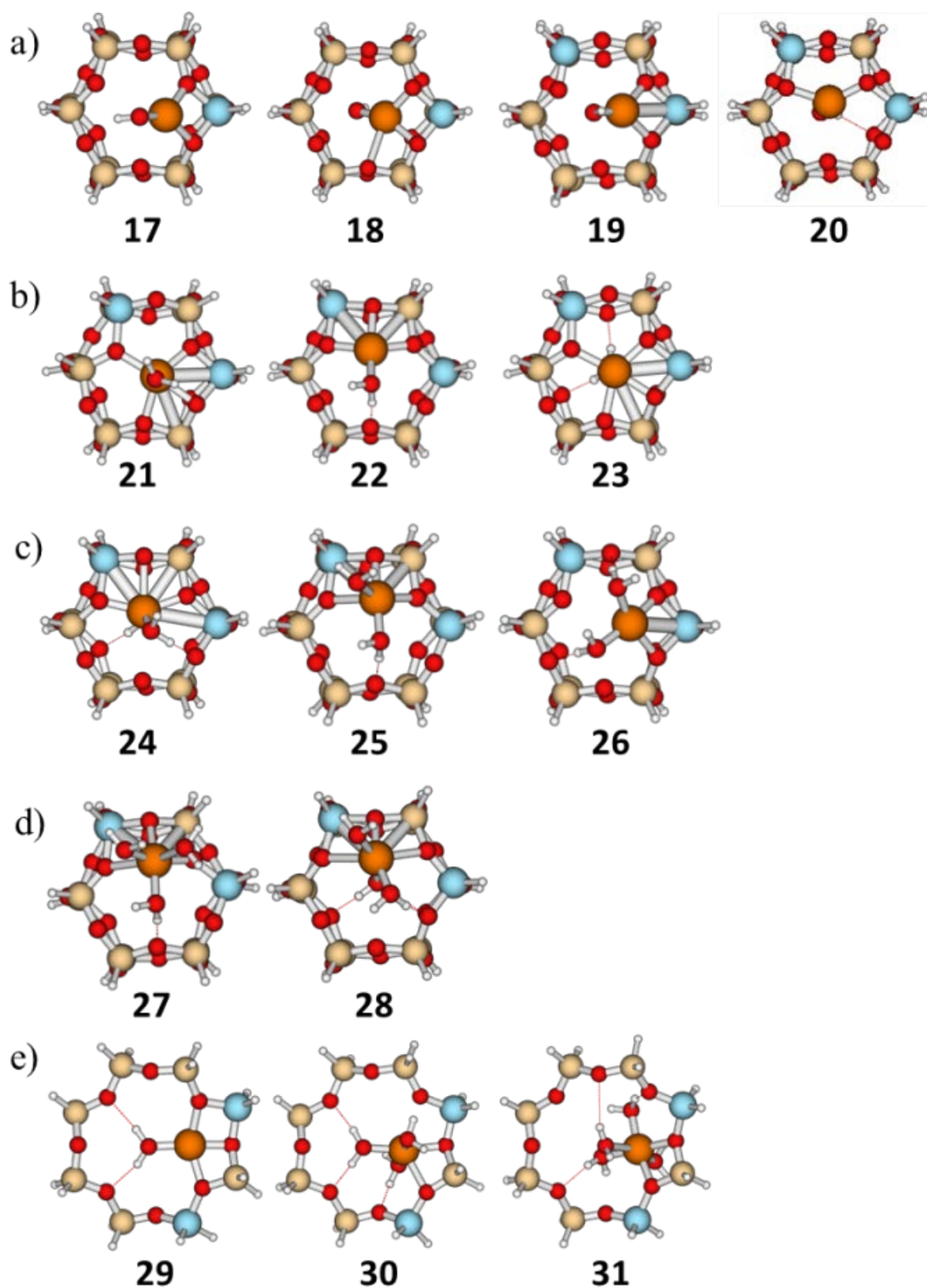
Figure 6. Optimized Cu-SSZ-13 structures of a) $[Cu^{2+}(OH^-)]^+$ species in 1Al and 2Al 6R-B2 distributions b) one water c) two water and d) three water additions to the 6R-B2 structure; and e) one, three and four water molecules in 8R. Si, Al, O, Cu and H atoms are depicted in sand, blue, red, orange and white, respectively.

41
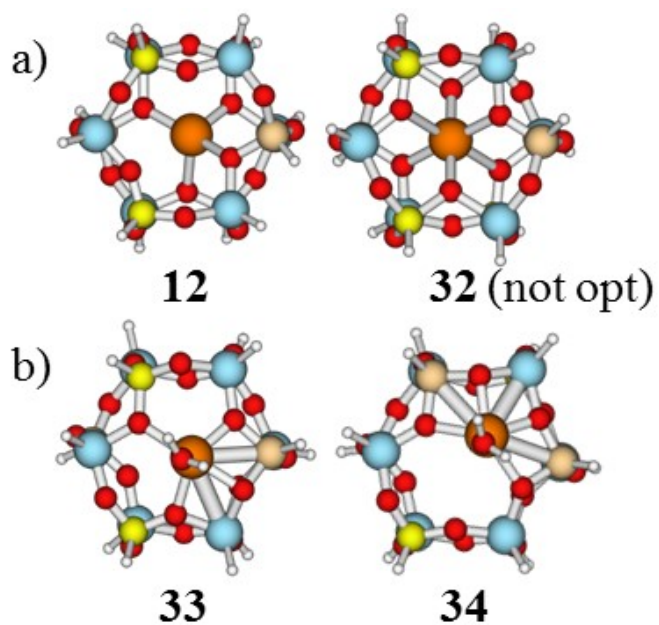
Figure 7. Optimized Cu-SAPO-34 structures of a) isolated Cu^{2+} species at **SI**, and b) $Cu(H_2O)(O_f)_4$ species at D6R and 6R-B1 **SII** sites. Si, Al, P, O, Cu and H atoms are depicted in sand, blue, yellow, red, orange and white, respectively.
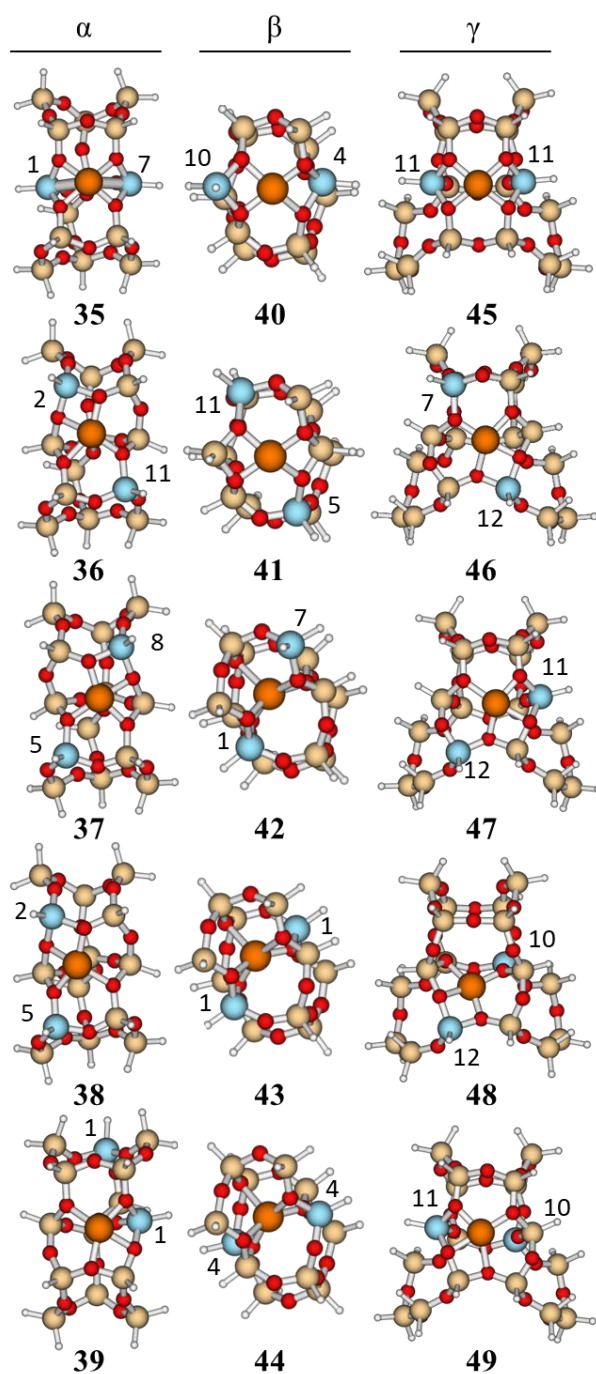
Figure 8. Optimized Cu-ZSM-5 structures of isolated Cu²⁺ species at α, β and γ sites in different distributions of two aluminum atoms. The specific crystallographic T-site for each Al atom is indicated. Si, Al, O, Cu and H atoms are depicted in sand, blue, red, orange and white, respectively.

C: $g_\parallel$ = 2.347 $A_\parallel$ = 493 MHz   H: $g_\parallel$ = 2.278 $A_\parallel$ = 539 MHz

G: $g_\parallel$ = 2.246 $A_\parallel$ = 503 MHz   I: $g_\parallel$ = 2.297 $A_\parallel$ = 437 MHz
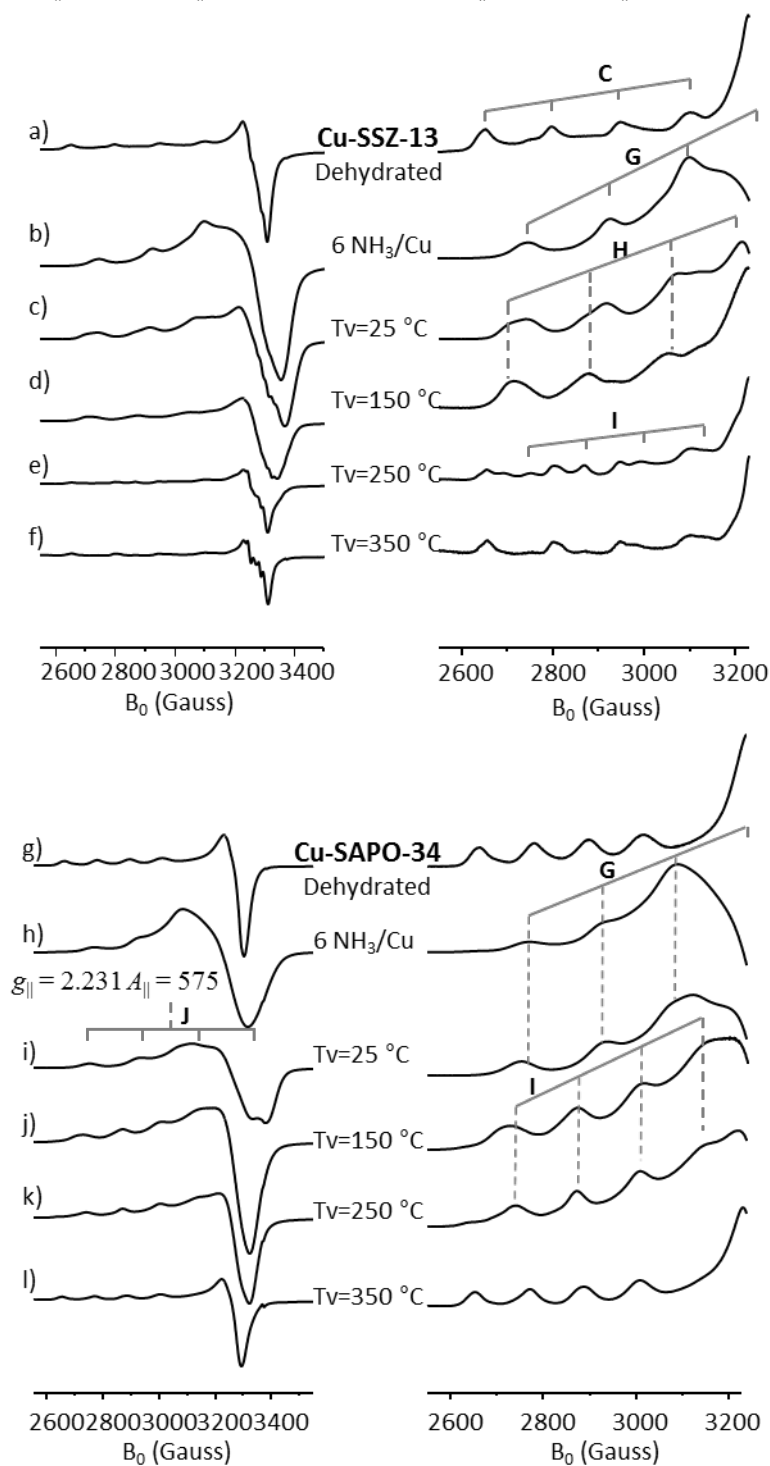
Figure 9. EPR spectra recorded at -170°C (left) and magnification of the low-field hyperfine structure (right) of zeolite Cu-SSZ-13 (a-f) and Cu-SAPO-34 (g-l) degassed at 450°C (a,g) followed by adsorption of 6NH$_3$/Cu atoms (b,h) and subsequent outgassing at increasing temperature (c-f, i-l).

44
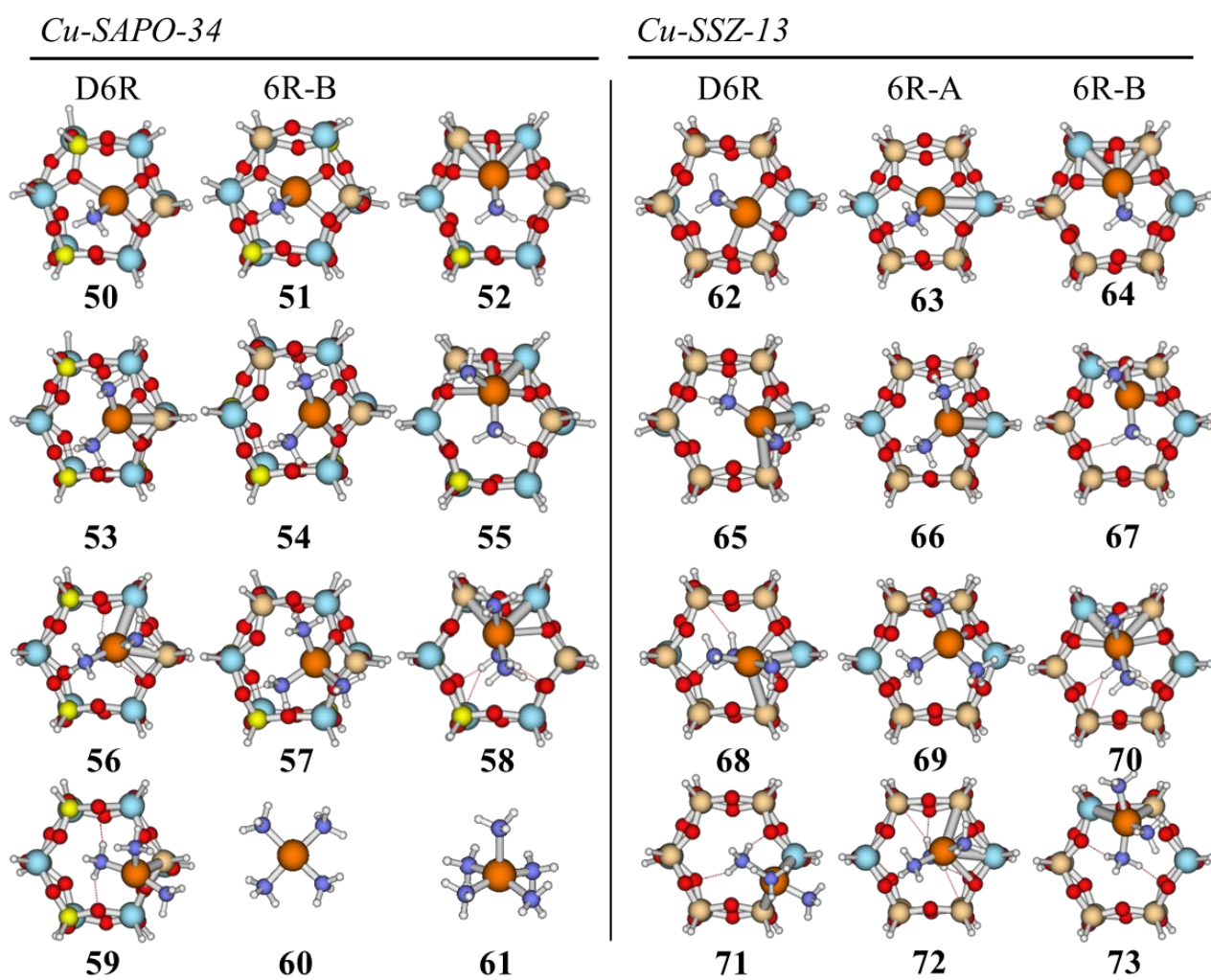
Figure 10. Optimized structures of one, two and three NH$_3$ molecules adsorbed on Cu-SAPO-34 and Cu-SSZ-13 catalysts, and [Cu(NH$_3$)$_4$]$^{2+}$ and [Cu(NH$_3$)$_5$]$^{2+}$ complexes. Si, Al, P, O, Cu, N and H atoms are depicted in sand, blue, yellow, red, orange, dark blue and white, respectively.
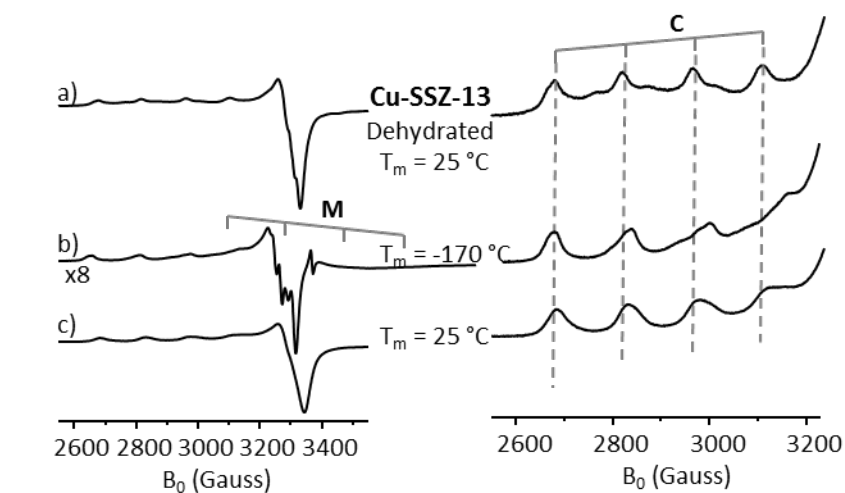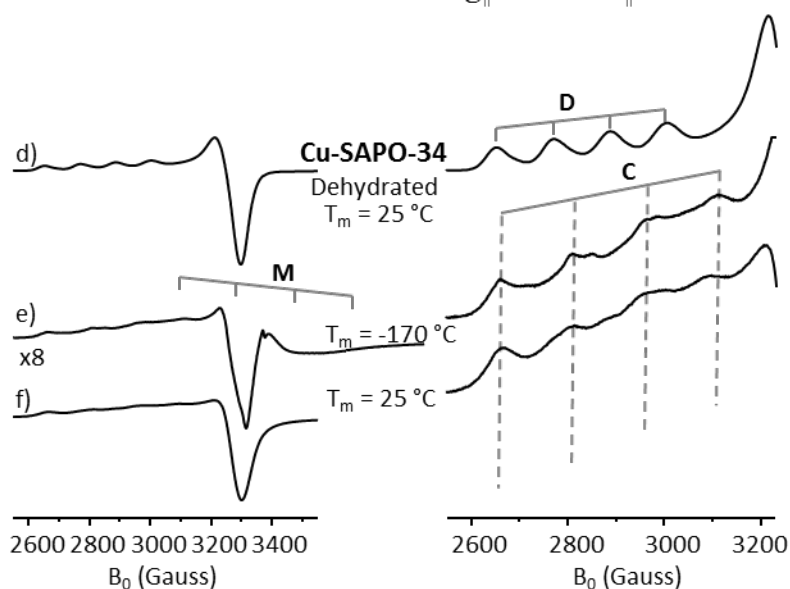
Figure 11. EPR spectra (left) and magnification of the low-field hyperfine structure (right) of a) Cu-SSZ-13 after dehydration at 450ºC b-c) after $2^{15}NO/Cu$ adsorption measured at -170 ºC and 25 ºC, and d) Cu-SAPO-34 after dehydration at 450ºC e-f) after $2^{15}NO/Cu$ adsorption measured at -170 ºC and 25 ºC.
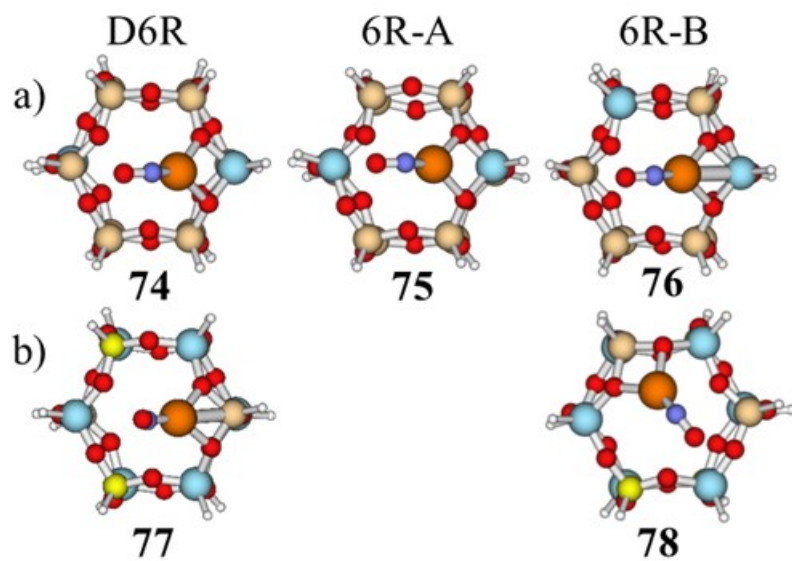
Figure 12. Optimized structures of one NO molecule adsorbed on a) Cu-SSZ-13 and b) Cu-SAPO-34. Si, Al, P, O, Cu, N and H atoms are depicted in sand, blue, yellow, red, orange, dark blue and white, respectively.
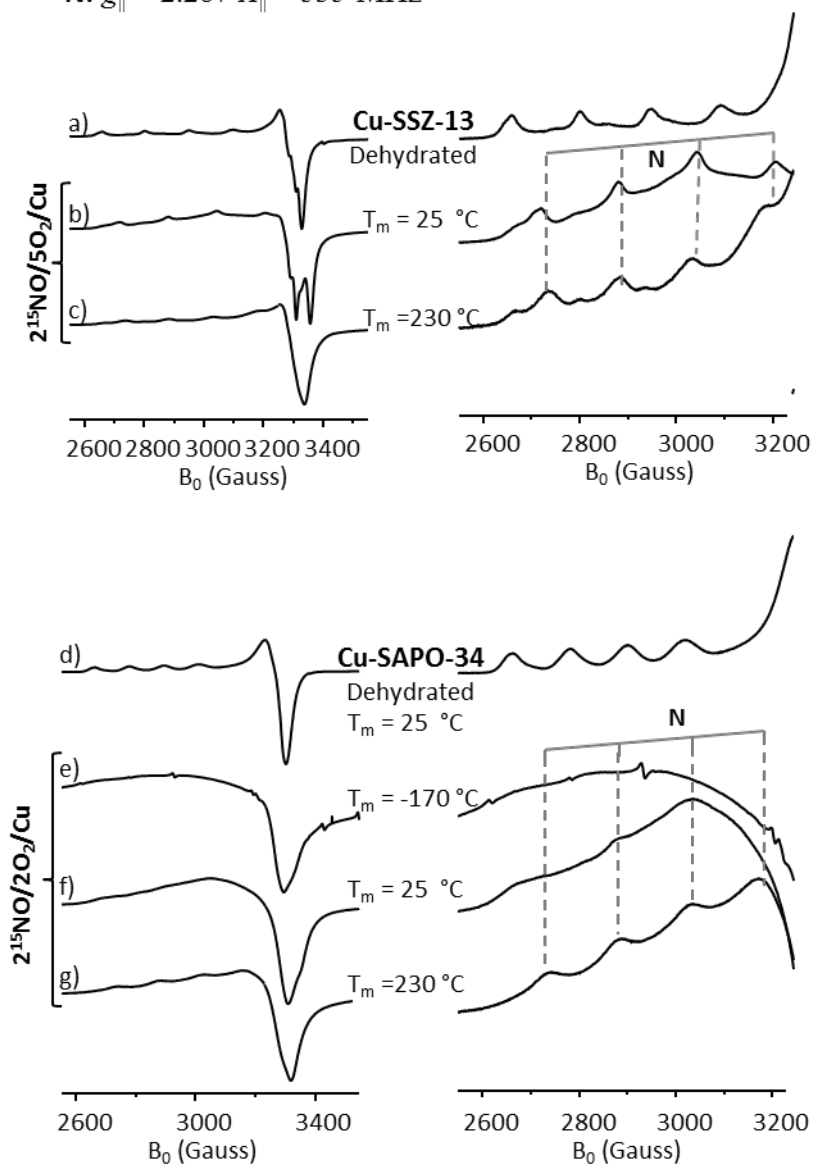
N: $g_\parallel = 2.287$ $A_\parallel = 535$ MHz

Figure 13. EPR spectra (left) and magnification of the low-field hyperfine structure (right) of a) Cu-SSZ-13 after dehydration at 450ºC and after $2^{15}NO/5O_2/Cu$ addition at b) 25 ºC, c) 230 ºC and d) Cu-SAPO-34 after dehydration at 450ºC, and after $2^{15}NO/2O_2/Cu$ addition at e) -170 ºC, f) 25 ºC, g) 230 ºC.
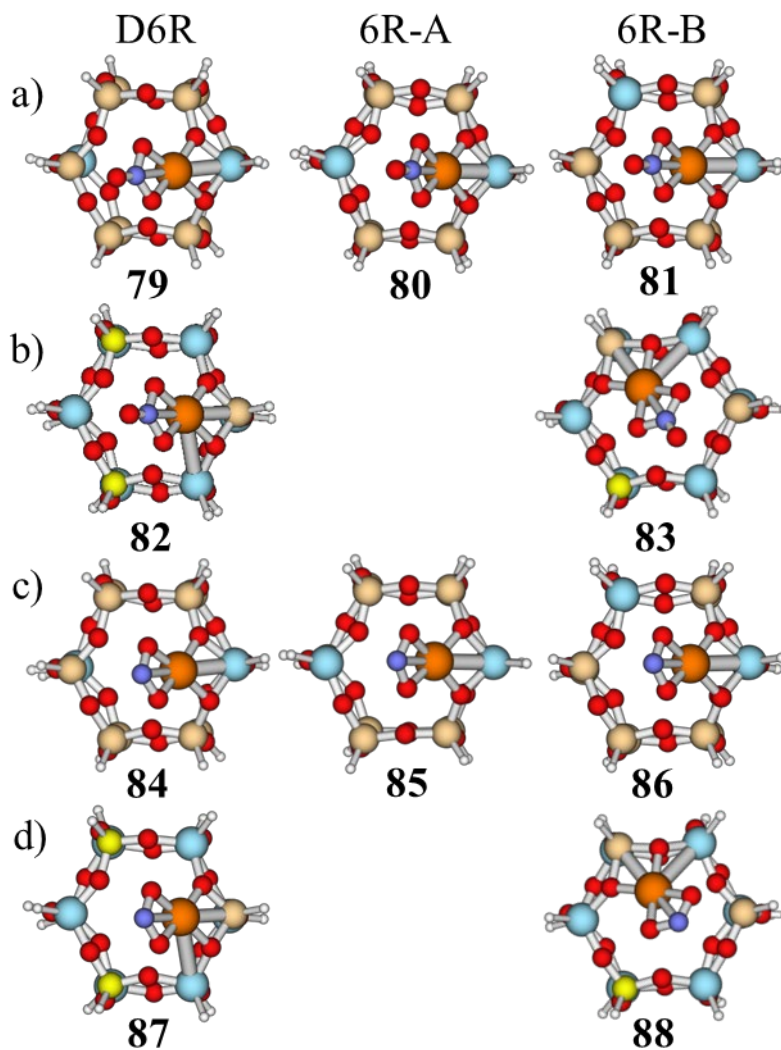
Figure 14. Optimized structures of nitrate species on a) Cu-SSZ-13 and b) Cu-SAPO-34 and of nitrite species on c) Cu-SSZ-13 and d) Cu-SAPO-34. Si, Al, P, O, Cu, N and H atoms are depicted in sand, blue, yellow, red, orange, dark blue and white, respectively.